

A Novel High-Resolution Alignment Technique for XFEL Using Undulator X-ray Beams

Bingxin Yang and Horst Friedrichs

Advanced Photon Source, Argonne National Laboratory, Argonne, IL 60439, USA

November 2005

Abstract

We propose a novel alignment technique utilizing the x-ray beam of an undulator in conjunction with pinholes and position-sensitive detectors for positioning components of the accelerator, undulator, and beamline in an x-ray free-electron laser. Two retractable pinholes at each end of the undulator define a stable and reproducible x-ray beam axis (XBA). Targets are precisely positioned on the XBA using a pinhole camera technique. Position-sensitive detectors responding to both x-ray and electron beams enable direct transfer of the position setting from the XBA to the electron beam. This system has the potential to deliver superior alignment accuracy ($1 - 5 \mu\text{m}$) in the transverse directions over a long distance (200 m or longer). It can be used on a smaller scale to accurately position assemblies pre-aligned using traditional alignment techniques. It can also be used to define the beam axis of electron beam-based alignment, enabling high reproducibility of the latter. This x-ray-based concept should complement the electron beam-based alignment and the existing survey methods to raise the alignment accuracy of long accelerators to an unprecedented level. Further improvement of transverse accuracy using x-ray zone plates will be discussed. We also propose a concurrent measurement scheme during accelerator operation to allow real-time feedback for transverse position correction.

1. Introduction

Several large-scale linear accelerator projects are under construction or have been proposed. The Linear Coherent Light Source LCLS [1] utilizes parts of the existing linear accelerator at SLAC followed by a 130-m-long undulator section with a 6.8-mm fixed gap. DESY is planning to build an XFEL [2] with a total length on the order of 3.3 km for multiple undulator sections of which the longest is about 300 m. The gap in this device varies from 6 to 20 mm depending on the undulator type utilized in each of the beamlines. A proposal by Spring8 to establish the SCSS [3] will use a 1-GeV, 55-m-long accelerator followed by a 22.5-m-long in-vacuum undulator section with a 3.7-mm gap. Finally, PAL at POSTECH in South Korea is proposing the PAL/XFEL [4] with a 60-m in-vacuum variable-gap undulator with a minimum gap of 3 mm.

These projects all require precision alignment of beamline components at unprecedented accuracy, including the vacuum chambers. In the LCLS, for example, many undulator components need to be aligned to better than $20 \mu\text{m}$ within a straight line designated to be the beam axis.

Using modern survey technology one can establish a control reference system with point accuracies of ± 150 to $\pm 300 \mu\text{m}$ depending on the size of the object. In long stretched objects such as linear accelerators or free-electron lasers (FEL), large-scale deviations due to the accumulation of small remaining systematic instrument errors and effects due to environmental

conditions can even exceed these tolerances and directly affect the positioning of the XFEL components. State-of-the art hydrostatic level sensors (HLS) deliver an accuracy of $\pm 5 \mu\text{m}$ and wire position sensors (WPS) are under development providing an accuracy of $\pm 1.5 \mu\text{m}$ over their respective measurement ranges. With these instruments it is possible to achieve relative alignment tolerances on the order of $\pm 25 \mu\text{m}$ or better when considering transfer errors from the monitors to the beam components. However, the accuracy of these devices is limited by the length of the object to be measured and on-axis alignment is not possible. Furthermore, two separate systems are required to position and monitor vertical and horizontal deviations.

Therefore, in 1968 W. Herrmannsfeldt [5] and others proposed and implemented a precision straight-line alignment system utilizing Fresnel lenses for the 3-km-long Stanford linear accelerator. The system uses a HeNe laser light source, a detector, and rectangular distance-dependent varying Fresnel lenses to project the source onto the detector. The accelerator is supported by 12-m-long linked girders with an integrated strongback for the accelerating structures and a 60-cm-diameter light pipe for the alignment system. At each girder link a Fresnel lens can be inserted into the light beam creating a diffraction pattern at the detector. Deviations relative to an initial straight-line setup using a well-defined Fresnel target and the detector zero position can be measured. Moving the strongback support with the Fresnel lens to the zero position, any link can be placed on-axis and with that the accelerating structure. The estimated transverse accuracy of this system is on the order of $\pm 25 \mu\text{m}$ over the length of the accelerator.

A similar system was proposed in 1990 by L. Griffith [6, 7] and his colleagues for the construction of an FEL at Lawrence Livermore Laboratory. This concept uses the Poisson spot created as a diffraction pattern by an opaque sphere substituting for a Fresnel lens to align the accelerator. It includes an elaborate feedback system to maintain the pointing direction of an expanded light beam and eliminates the need for inserting and removing reference targets as required in the SLAC design, as many spheres can occupy the cross section of the light beam. This system was designed to provide transverse positioning on the order of $\pm 25 \mu\text{m}$ over a 300-m-long FEL.

Similar to these previous authors, we believe that the optical technique is preferred since the photons travel in straight lines in vacuum and their trajectory curves less than 1 prad/km as a result of earth's gravity. The above techniques have two major drawbacks. First, they establish straight lines nearly a meter away from the main electron beam axes, and the transfer error is not negligible. Second, the diffraction of light beam also limits the working distance of techniques based on visible light. If we choose a cylindrical axis with the z -axis along the propagating beam axis and its origin located at the beam waist, then the intensity distribution of a simple, lowest-order Gaussian light beam [8] is given by

$$|E(r, z)|^2 = \frac{\sigma(0)^2}{\sigma(z)^2} |E(r, 0)|^2 e^{-\frac{1}{2} \left(\frac{r}{\sigma(z)} \right)^2}, \quad (1.1)$$

where the rms beam radius σ is a function of the distance z and the Rayleigh length $z_R = \sigma_0^2 / \lambda$,

$$\sigma(z) = \sigma(0) \sqrt{1 + \frac{z^2}{z_R^2}} = \sigma_0 \sqrt{1 + \frac{z^2}{z_R^2}}. \quad (1.2)$$

For visible light with a wavelength $\lambda = 0.632 \mu\text{m}$ and a Rayleigh length of 100 m, the rms radius of the beam waist reaches $\sigma_0 = \sqrt{\lambda z_R} = 3.2 \text{ mm}$. The full beam size at a Rayleigh length away is therefore in the range of centimeters and a visible light beam would not be able to travel freely inside the undulator or accelerator vacuum chamber.

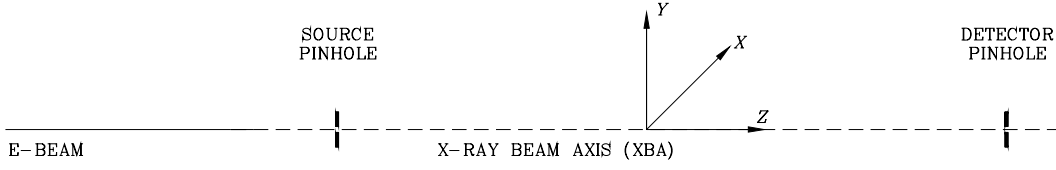
From Eq. (1.2), we can see that the beam diameter remains small for x-ray photons over a long distance when the wavelength is in the range of 0.02 – 2 nm. In this work we propose a procedure for utilizing x-rays from a dedicated alignment undulator source and the diffraction pattern of pinholes to align XFEL beamline components. We also propose to establish the x-ray beam axis (XBA) coincident with the main electron beam axis (EBA). We will start by describing the proposed alignment procedure using x-ray pinholes as alignment targets in Section 2, and then estimate the alignment accuracies using geometric and wave optics in Section 3. We will discuss how to choose suitable x-ray optical components, from the source to the detector for an x-ray alignment system in Section 4. We discuss offline and online fiducialization issues in Section 5, other issues in Section 6, and summarize the paper in Section 7. Most of our discussion will be based on the geometry of LCLS, but it can be easily extended to other large-scale accelerator projects.

2. Alignment procedure using x-ray optics

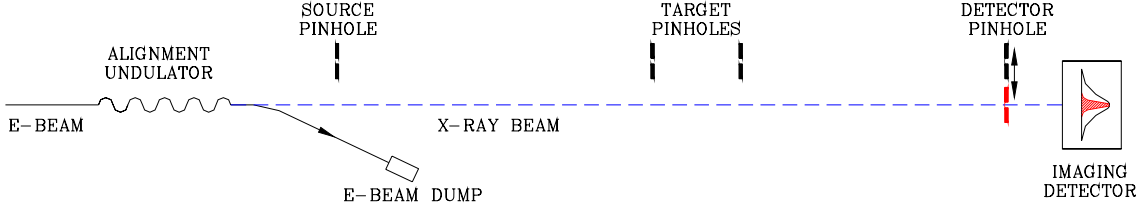
In this section we describe the proposed procedures for setting up the optics and aligning x-ray pinholes on a straight line. Figure 2.1 shows the schematics of the x-ray instrument: An alignment undulator is located 20 – 30 m upstream of the main undulator beamline to be positioned. A retractable x-ray pinhole (source pinhole), is located midway between the alignment undulator and the beginning of the main undulator beamline. It is used to define the source point for the alignment. An x-ray imaging detector is located 10 m or more downstream of the main undulator beamline. A second retractable x-ray pinhole (detector pinhole) is located immediately upstream of the detector. It will be used to define the center of the detector plane. The two x-ray pinholes, when both are inserted, define a straight line, which will be referred to as the x-ray beam axis (XBA). In addition, every component to be aligned with the x-ray beam will need a retractable pinhole as an alignment target. The location of these targets, in their inserted position, should either be fiducialized offline to the critical dimensions of the component on the bench, or with the electron and x-ray beams via an online process (Section 5).

2.1 Setup of the x-ray beam axis (XBA) and primary coordinate system

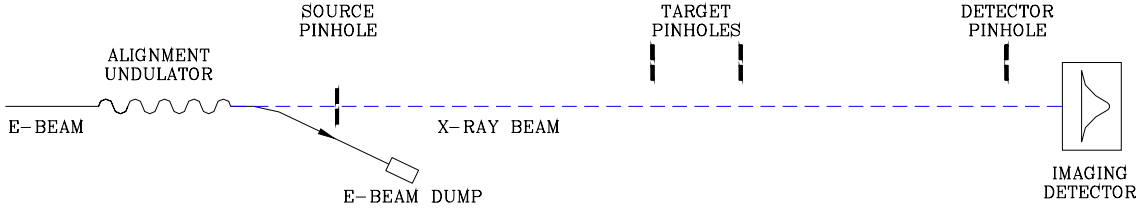
The reference XBA is set up by conventional survey method: use the survey tools to set up the source and detector pinholes, both at inserted positions, onto the design electron beam axis at the best achievable accuracy (Fig. 2.1A). Once the two pinholes are set, the conventional survey monument network becomes secondary. The primary coordinates are now uniquely defined by the following rules: The z -axis or the XBA is the straight line linking the centers of the two pinholes, from the source to the detector. The Oyz plane is defined by the triangle formed by the center of the earth and the two pinholes. The y -axis is perpendicular to the z -axis, and pointing away from the center of the earth, although not necessarily passing through it. The x -axis is defined by the right hand rule, $\hat{\mathbf{x}} = \hat{\mathbf{y}} \times \hat{\mathbf{z}}$, and is the only horizontal line perpendicular to the z -axis.



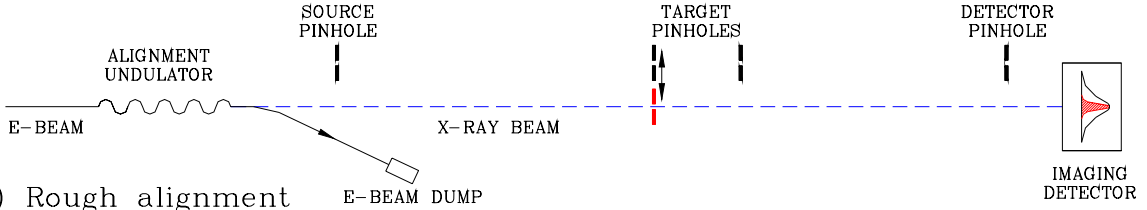
(A) Definition of coordinates



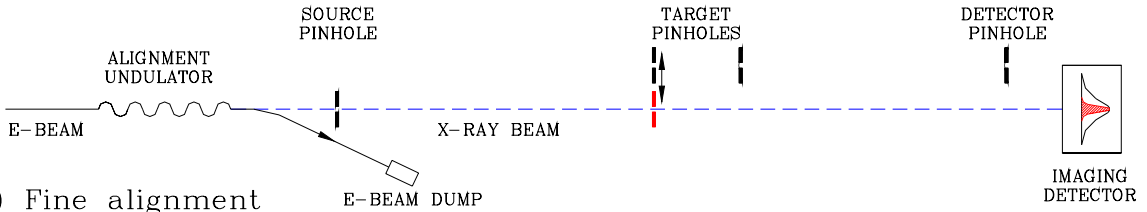
(B) Setup detector and beam direction



(C) Setup source position



(D) Rough alignment



(E) Fine alignment

Figure 2.1: Schematics showing the alignment procedure of x-ray pinholes: (A) Definition of the XBA coordinates, (B) setup detector with a retractable (detector) pinhole, (C) setup x-ray undulator source position, (D) rough alignment of target pinhole one by one, and (E) fine alignment of pinholes.

2.2 Align undulator source to the XBA and fiducialize the detector

Setting up the undulator, or putting the electron trajectory in the undulator on the XBA, requires the iteration of the following two steps until convergence:

(A) Setting up the undulator beam direction

Retract the source pinhole and steer the electron beam in the alignment undulator so that the x-ray spot is centered on the detector. Insert and retract the detector pinhole between steerings to mark the center of the detector several times. This helps to steer the undulator beam to be parallel to the XBA (Fig. 2.1 B).

(B) Setting up the undulator source position

Retract the detector pinhole and insert the source pinhole. Translate the electron beam in the alignment undulator so that the x-ray spot is centered on the detector and its intensity is maximized (Fig. 2.1 C). This helps position the undulator source point onto the XBA.

2.3 Rough alignment

The goal of the rough alignment is to bring the center of the component or target pinholes close to the x-ray beam axis so fine alignment can be performed. The procedure has two steps:

- (A) Retract both source and detector pinholes after the undulator has been aligned.
- (B) Insert each target one at a time and move it to center the beam spot on the detector plane (Fig. 2.1 D).

The alignment resolution and accuracy will be affected by the size and transverse stability of the electron beam.

2.4 Fine alignment

In the fine alignment step, we use the source pinhole as a secondary source, which is small in size and stable in the transverse position. The procedure is similar to that of the rough alignment:

- (A) Insert the source pinhole and check the center position on the detector.
- (B) Insert each target one at a time and move it with the attached beamline component to center the x-ray beam spot on the detector plane. Average over many shots if necessary to improve photon statistics (see Fig 2.1 E).

While the size and transverse stability of the electron beam affects the intensity at the detector plane, the resolution and accuracy of this fine and final alignment is determined only by the optics. This will be the subject of the next section.

3. Alignment accuracy and instrument resolution

In this section, we estimate the alignment accuracy of the target pinholes in three steps:

- (1) Calculate the beam spot size and profile at the detector plane produced by a point source,

- (2) calculate the beam spot size and profile at the detector plane produced by an extended source, and
- (3) convert the measured beam size as the alignment accuracy of the pinhole using the optical geometry.

3.1 Pinhole camera resolution at the detector plane

X-ray pinholes have been used for measuring electron beam sizes for some years. Their performance is best modeled by Fresnel diffraction [9-11]. Figure 3.1 shows a typical geometry of a pinhole camera, with a pinhole located at a distance S_1 from the source, and an x-ray imaging camera at a distance S_2 from the pinhole. The Fresnel number defined as the number of Fresnel zones, given by $F = a^2 / \lambda f$ is a key parameter in the model, where a is the radius of the circular pinhole, λ is the wavelength of the light, and the distance f is given by $\frac{1}{f} = \frac{1}{S_1} + \frac{1}{S_2}$.

In this coordinate system, we label all transverse coordinates on the source plane with subscript 0, those coordinates on the pinhole plane with subscript 1, and those coordinates on the image plane with subscript 2, as shown in Figure 3.1. For large Fresnel numbers ($F \gg 1$) the behavior of the optical system can be approximated by geometric optics. For a point source, the beam spot on the detector plane is a disc with a radius of $a_2 = (M + 1)a$, where $M = S_2 / S_1$ is the magnification of the optical system. When integrating the measured beam intensity in the y -direction, the resultant beam profile in the x -direction has an rms width of $(M + 1)a/2$. Fitting the profile to a Gaussian function, however, gives a width of

$$\sigma_{2,geo} = 0.59a_2 = 0.59(M + 1)a. \quad (3.1)$$

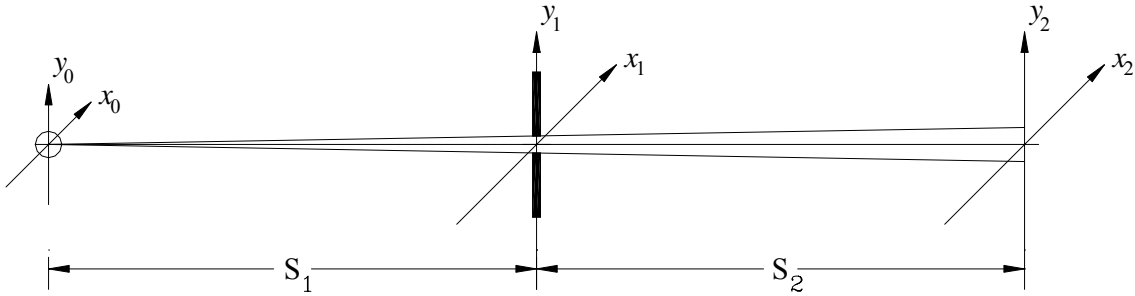


Figure 3.1: Schematics of a pinhole camera with a point source. Projection of the pinhole on the image plane shows a magnified area.

For small Fresnel numbers ($F \ll 1$) the behavior of the optical system can be approximated by Fraunhofer diffraction, and the diffraction pattern is given by the Airy disk,

$$I(\theta) = I_0 \left[\frac{J_1(ka \sin \theta)}{ka \sin \theta} \right]^2, \text{ where the wave vector is given by } k = \frac{1}{\lambda} = \frac{2\pi}{\lambda}. \text{ At a distance } S_2 \text{ from}$$

the pinhole, the intensity distribution is

$$I(r_2) = I_0 \left[\frac{J_1(kar_2/S_2)}{kar_2/S_2} \right]^2, \quad (3.2)$$

where $r_2 = \sqrt{x_2^2 + y_2^2}$ is the radial distance from the axis. The annular diffraction pattern $I(r_2)$ can be used to derive the integrated x-profile:

$$P(x_2) = \int_{-\infty}^{\infty} I(r_2) dy_2 = 2 \int_{|x_2|}^{\infty} \frac{I(r_2)r_2}{\sqrt{r_2^2 - x_2^2}} dr_2. \quad (3.3)$$

The profile features a central peak with several side peaks and can be fitted to a Gaussian

function $P_{fit}(x) = P_0 e^{-\frac{x^2}{2\sigma_{2,diff}^2}}$, with $\sigma_{2,diff} = 1.31 \cdot \lambda S_2 / a$. In a popular hybrid model, the approximate beam profile width at the detector plane is given by adding the two widths together in quadrature [12, 13],

$$\sigma_{2,reso}^2 = \sigma_{2,geo}^2 + \sigma_{2,diff}^2 = 0.35(M+1)^2 a^2 + 1.72 \frac{\lambda^2 S_2^2}{a^2}, \quad (3.4)$$

or

$$\frac{\sigma_{2,reso}^2}{(M+1)^2 \lambda f} = 0.35F + \frac{0.044}{F}. \quad (3.5)$$

Figure 3.2 shows the beam sizes at the detector plane for geometric projection, Fraunhofer diffraction, and the hybrid model. However, the more accurate Fresnel diffraction calculation for circular apertures (Appendix A) shows that the point spread function (PSF) profile width is narrower than that predicted by Eq. (3.5). An approximation to the beam size is given by the following fit:

$$\frac{\sigma_{2,reso}^2}{(M+1)^2 \lambda f} = \frac{F}{3} \left(1 + \frac{1.5}{F} \right)^{-1} + 0.044 \left(0.3 + \frac{1}{F} \right). \quad (3.6)$$

From Fig. 3.2, we can also see that for large apertures ($F > 0.38$), the Fresnel diffraction PSF profile is always narrower than that of the geometric projection

$$\sigma_{2,reso} \leq \sigma_{2,geo} = 0.59(M+1)a, \quad (F \geq 0.38). \quad (3.7)$$

In this regime, we can use geometric projection for our semi-quantitative discussion, with the comforting thought that Fresnel diffraction will only make the beam size smaller.

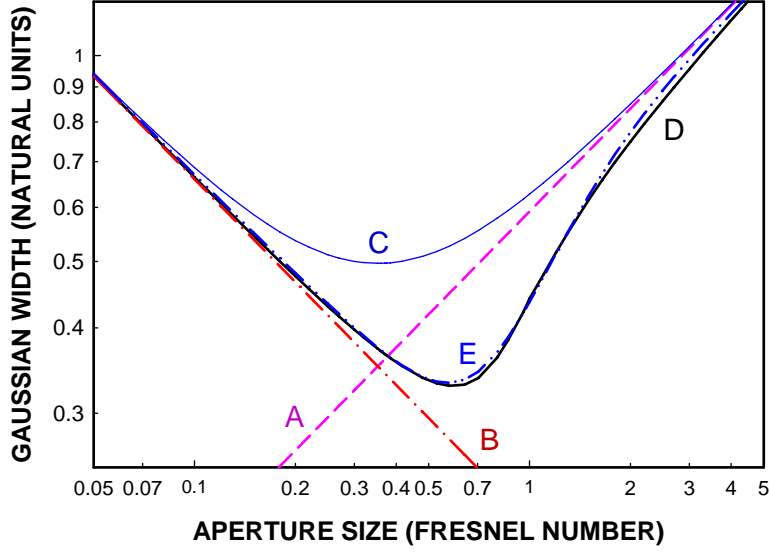


Figure 3.2: Calculated Gaussian width of PSF profiles of a pinhole camera with different models: (A) geometric projection, (B) Fraunhofer diffraction, (C) hybrid model: quadrature sum of the previous two, (D) monochromatic Fresnel diffraction, and (E) fit to D, as in Eq. (3.6).

3.2 Beam profile size for an extended source

When we have an extended source with a finite source size σ_{x0} , the beam spot on the detector plane is larger than that of a point source. Let us consider the extended source as a collection of point sources in a Gaussian distribution,

$$\rho(x_0, y_0) = \rho_0 e^{-\frac{1}{2} \left(\frac{x_0^2}{\sigma_{x0}^2} + \frac{y_0^2}{\sigma_{y0}^2} \right)}. \quad (3.8)$$

For each point source located off axis by x_0 , its beam spot on the detector plane will be centered on $x_2 = Mx_0$. Summing the contribution of all point sources amounts to calculating the convolution of the Gaussian profile with the pinhole camera PSF profile. The total beam profile size at the detector plane is thus

$$\sigma_2^2 = \sigma_{2, \text{reso}}^2 + M^2 \sigma_{x0}^2. \quad (3.9)$$

3.3 Alignment accuracy of the pinhole position

We now use the centroid of the beam spot at the detector plane as an indication of whether the pinhole is centered on the optical axis. The error of positioning the centroid of a Gaussian peak is normally a fraction of the peak width, i.e. $\eta\sigma_2$, where $\eta = 0.03 \rightarrow 0.2$ depending on the quality of the photon measurements. Adding the fiducialization error $\eta(0.59a_D)$ from a detector pinhole of radius a_D , the total uncertainty is $\eta\sqrt{\sigma_2^2 + (0.59a_D)^2}$. For a pinhole displacement of Δx_1 , the center of the beam spot on the detector plane moves by

$$\Delta x_2 = (M + 1)\Delta x_1. \quad (3.10)$$

Hence the rms alignment accuracy at the pinhole location is given by

$$\delta_{align} = \frac{\eta}{M+1} \sqrt{\sigma_2^2 + 0.35a_D^2}, \quad (\eta = 0.03 - 0.2). \quad (3.11)$$

Next we introduce five new variables, the total beamline length $S = S_1 + S_2$, the relative target position $z = S_1/S$, the minimum target Fresnel number $F_m = 4a^2/\lambda S$, the scaled source size $F_0 \equiv 4a_0^2/\lambda S$, and the scaled detector size $F_D \equiv 4a_D^2/\lambda S$. We then rewrite Eq. (3.11) as

$$\delta_{align} = \eta \frac{\sqrt{\lambda S}}{4} g(z), \quad (\eta = 0.03 - 0.2), \quad (3.12)$$

where

$$g(z) = 1.18 \left\{ \frac{0.95F_m^2}{F_m + 6z(1-z)} + 0.15z(1-z) + \frac{2}{F_m} z^2(1-z)^2 + (1-z)^2 F_0 + z^2 F_D \right\}^{1/2}. \quad (3.13)$$

Figure 3.3 shows the function $g(z)$ for a near-zero source and size ($F_0 = F_D = 0.01$). It can be seen that when F_m is in the range of $0.3 - 0.45$, the Fresnel diffraction pattern is at its minimum width for most of the beamline, and a good resolution is obtained over the entire beamline. Figure 3.4 shows the dependence of function $g(z)$ on the source size for a fixed, near-ideal target size ($F_m = 0.35$). It can be seen that when F_0 is in the range of $0.3 - 0.5$, the function $g(z)$ is fairly flat and less than one. In short, the ideal operating condition can be represented as

$$\left. \begin{array}{l} F_0 = 0.50 \pm 0.10 \\ F_m = 0.36 \pm 0.05 \\ F_D = 0.50 \pm 0.10 \end{array} \right\}, \text{ or } \left. \begin{array}{l} a_0 = (0.35 \pm 0.04) \sqrt{\lambda S} \\ a = (0.30 \pm 0.02) \sqrt{\lambda S} \\ a_D = (0.35 \pm 0.04) \sqrt{\lambda S} \end{array} \right\}, \quad (3.14)$$

with resulting alignment accuracy

$$\delta_{align} \approx \eta \frac{\sqrt{\lambda S}}{4}, \quad (\eta = 0.03 - 0.2). \quad (3.15)$$

Take the LCLS undulator as an example [14]: $\lambda = 0.5 \text{ \AA}$, $S = 200 \text{ m}$, and $\eta = 0.1$. The ideal target and source pinhole radii are $30 \pm 2 \text{ (}\mu\text{m)}$ and $32 \pm 4 \text{ (}\mu\text{m)}$, respectively. The estimated positioning accuracy by Eq. (3.15) is

$$\delta_{align} \leq 0.1 \times 25 (\mu\text{m}) = 2.5 (\mu\text{m}). \quad (3.16)$$

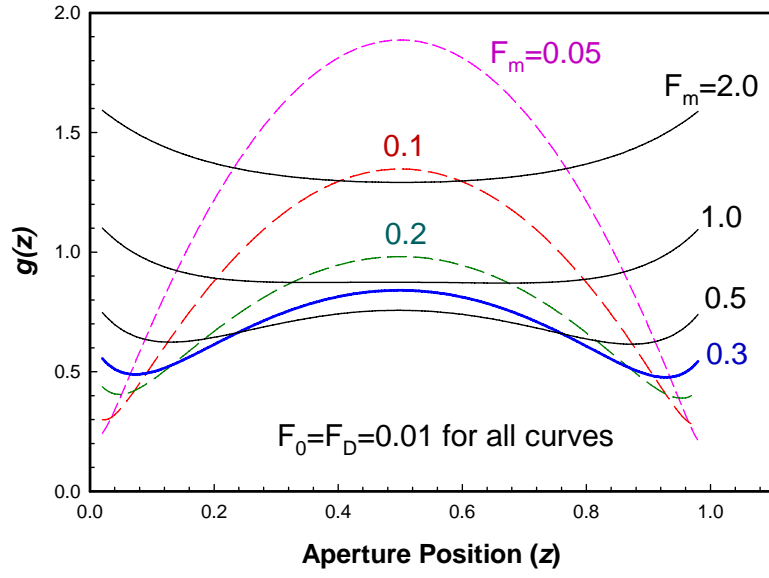


Figure 3.3: Function $g(z)$ for different aperture sizes with near-zero source size ($F_0 = F_D = 0.01$).

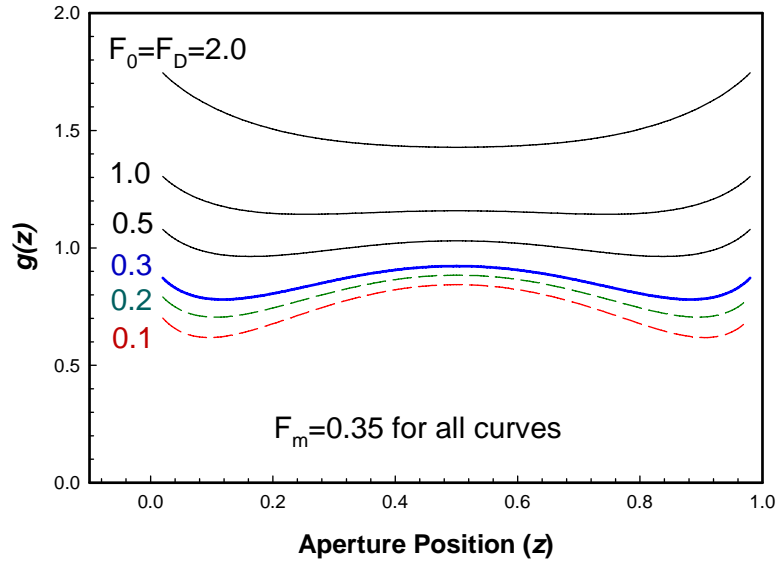


Figure 3.4: Function $g(z)$ for different source sizes with near-ideal target size ($F_m = 0.35$).

4. X-ray optics issues

In the last section, we analyzed the performance of an ideal pinhole with a monochromatic light source. In the x-ray region, such idealized conditions may not always be realized. The source usually emits photons in many wavelengths, and the pinhole is usually made of materials partially transparent. Furthermore, the response of the detector is a function of photon energy, which can be modified by adding transmission filters and reflection mirrors. In this section, we will discuss how to choose pinhole materials, to tailor detector system response, and to specify undulator sources for precision alignment.

4.1 Pinhole

The intensity of a monochromatic x-ray beam attenuates exponentially into a uniform medium [15]. The fraction of flux transmitted through a foil of thickness t is given by

$$\eta_t = e^{-\mu_M \rho_M t}, \quad (4.1)$$

where μ_M is the mass attenuation coefficient and ρ_M is the density of the metal. We note that a pinhole made with semi-transparent foil will have a peak-to-background ratio of $\sim 1/\eta_t$ immediately downstream of the pinhole.

From the last section, we note that if we are using the optimum aperture size, the x-ray beam spot on the detector plane is usually narrower than that of the geometric projection of the pinhole aperture, and the profile peak is higher than that of the geometric projection. Hence for estimating the signal-to-background ratios, we can safely use the approximation of the geometric projection, where the ratio is preserved downstream of the aperture. A simple rule of thumb can be given as

$$\eta_t \leq \frac{1}{r_{S/B}^{(\min)}}, \quad (4.2)$$

where $r_{S/B}^{(\min)}$ is the minimum signal-to-background ratio the experiment needs. The above two equations can be combined to give

$$t \geq t_{\min} \left(r_{S/B}^{(\min)} \right) \equiv \left(\mu_M \rho_M \right)^{-1} \ln r_{S/B}^{(\min)}, \quad (4.3)$$

where t_{\min} is the minimum thickness for the pinhole foil. Table 4.1 shows the minimum foil thickness for several desirable signal-to-background ratios.

We can draw the following conclusions from examining Table 4.1:

- (1) If we accept a background at 10% level, a 0.5-mm-thick foil (Ta, W, or Au) would be sufficient for applications using photon energy up to 110 keV.
- (2) Similarly, a 0.25-mm-thick foil would be sufficient for applications using photon energy up to 50 keV.
- (3) These requirements can be further relaxed for many polychromatic sources. For example, for an x-ray source with photon energy in the region of 10 to 100 keV, a 0.25-mm-thick foil would likely be sufficient since most low-energy photons will be blocked by the foil.

Figure 4.1 shows the fraction of x-ray transmission through some tantalum, tungsten, and gold foils in the photon energy range of 5 to 200 keV [16]. We showed in the example in the previous section that suitable pinholes for target and source apertures have diameters of 50 μm or larger. Hence the pinhole aspect ratio is less than ten. Fabrication of these pinholes is well within today's technological capabilities.

Table 4.1: Required thickness of selected metal foil for minimum signal-to-background ratio
(X-ray photon energy < 100 keV)

Minimum Signal / Background ratio	Tantalum (Ta) (Density = 16.8 g/cm ³) $(\mu_M \rho_M)^{-1} = 0.218$ mm at the K-edge 66.70 keV	Tungsten (W) (Density = 19.25 g/cm ³) $(\mu_M \rho_M)^{-1} = 0.202$ mm at the K-edge 69.33 keV	Gold (Au) (Density = 19.32 g/cm ³) $(\mu_M \rho_M)^{-1} = 0.232$ mm at the K-edge 79.40 keV
3	0.24 mm	0.22 mm	0.25 mm
5	0.35 mm	0.33 mm	0.38 mm
10	0.50 mm	0.47 mm	0.53 mm
50	0.85 mm	0.78 mm	0.91 mm
100	1.00 mm	0.93 mm	1.06 mm
1000	1.51 mm	1.36 mm	1.59 mm

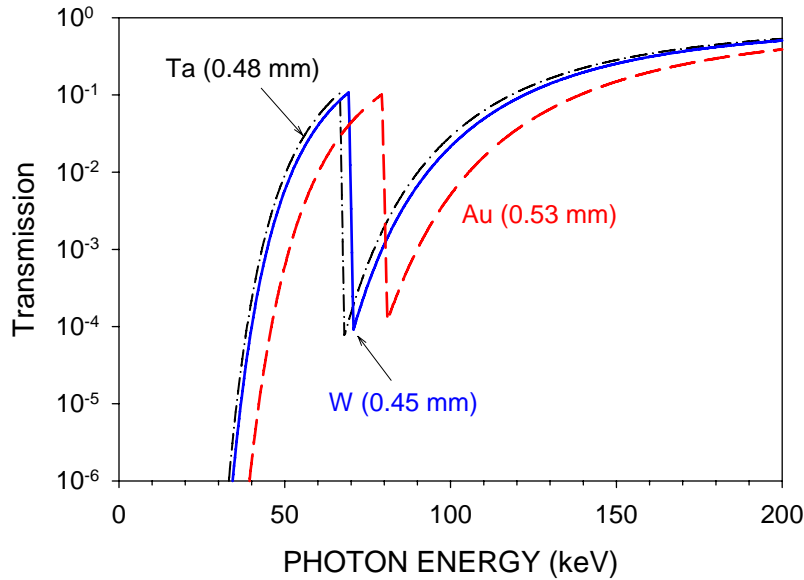


Figure 4.1: Transmission of x-rays through selected metal foils: tantalum (0.48 mm), tungsten (0.45 mm), and gold (0.53 mm). The foils are chosen such that the transmission is always under 10% up to an x-ray photon energy of 100 keV.

4.2 Detector system

For x-ray alignment we can use imaging and non-imaging detectors. Imaging detectors use two-dimensional arrays to acquire a map of photon flux. One popular approach is to use an x-ray scintillator (YAG, for example) to convert the x-ray to visible light and then use optical lenses and cameras to acquire the image. The alternative is to use a pixilated x-ray detector, although

most types of pixilated x-ray detectors are susceptible to radiation damage at high flux. The non-imaging detectors are commonly referred to as position sensitive detectors (PSD). While many designs exist, the majority of them operate on the principle of dividing the signal of the detector into several parts or quadrants, with their fractions of the signal dependent on the position of the beam centroid, such that the beam position is proportional to the ratio of the difference between the two opposing parts over their sum. The resolution of the PSD is often a small fraction (one to several per cent) of the beam size.

A detector responding to only a narrow band of x-ray wavelength is often useful in improving the signal-to-background ratio. Filters upstream of the detector can be used to remove unwanted long wavelength photons and stray light. Figure 4.2 shows the transmission spectra of several commonly available filters using program XOP [16].

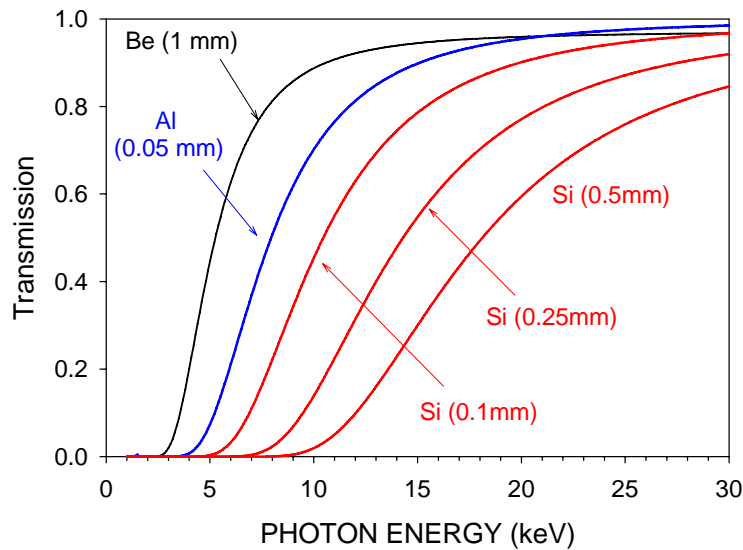


Figure 4.2: Transmission spectra of x-rays through selected filter foils.

Mirrors can also be used to remove unwanted high-energy photons. Figure 4.3 shows typical reflectivity curves of a metal coated mirror. As a rule of thumb, the cut-off photon energy can be written as

$$\omega_c \approx C/\theta, \quad (4.4)$$

where θ is the grazing incidence angle in mrad, and C is a material-dependent constant, several of which are listed in Table 4.2. An alternative approach, though less effective, is to reduce the detector's response to high-energy photons by making the detector from thin low- Z material, near or below two absorption lengths at the working photon energy.

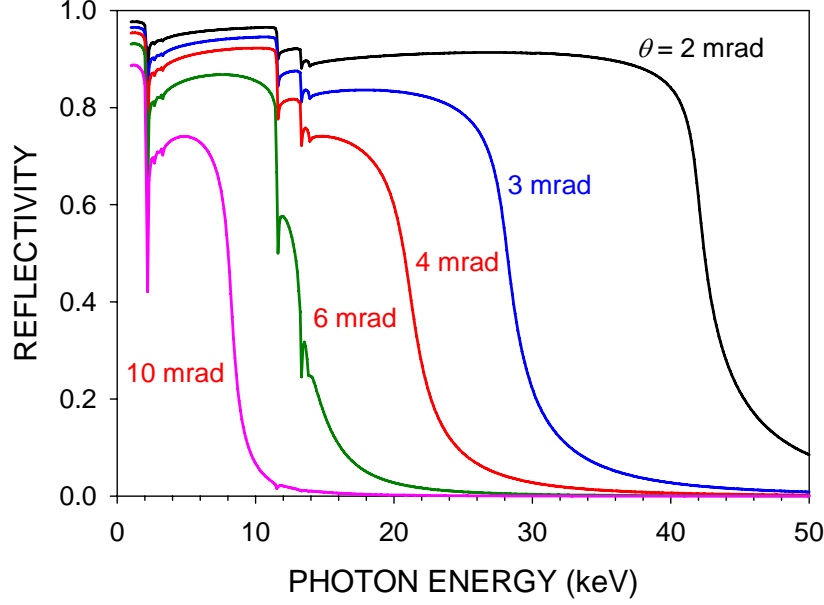


Figure 4.3: Reflectivity spectra of a Pt-coated mirror (bulk density assumed).

Table 4.2: Calculated mirror constant C for selected metals (bulk density assumed)

Metal	Re	Au	Pt
Mirror constant (keV-mrad)	66	80	85

4.3 X-ray sources

The only x-ray source for alignment over a long distance is an undulator. An undulator has a fundamental frequency

$$\omega_1 \equiv \frac{4\pi c \gamma^2}{\lambda_u (1 + K^2/2)}, \quad (4.5)$$

where λ_u is the magnetic period length of the undulator, γ is the Lorentz factor of the electron, and K is the undulator magnetic parameter. On the beam axis, the photons aggregate in regions near odd multiples of ω_1 , with the on-axis brilliance given by [15-17]

$$\frac{d^2 F_n}{d\phi d\psi} [ph/s/mr/0.1\%BW] = 1.744 \times 10^{14} N^2 E^2 [GeV] I [A] f_n(K) S_N(\omega), \quad (n = 1, 3, \dots) \quad (4.6)$$

where

$$f_n(K) = \frac{n^2 K^2}{(1 + K^2/2)^2} \left\{ J_{\frac{n-1}{2}} \left[\frac{nK^2}{4(1 + K^2/2)} \right] - J_{\frac{n+1}{2}} \left[\frac{nK^2}{4(1 + K^2/2)} \right] \right\}^2, \quad (4.7)$$

and the on-axis photon spectrum is a narrow spike (sinc function),

$$S_N(\omega) = \left[\frac{\sin\left(nN\pi \frac{\omega - \omega_1}{\omega_1}\right)}{N \sin\left(n\pi \frac{\omega - \omega_1}{\omega_1}\right)} \right]^2. \quad (4.8)$$

The integrated photon intensity through a pinhole aperture of $\Delta\Omega$ [μrad^2] near each order is approximately given by

$$\begin{aligned} F_n^{(o)}[ph/order] &= \int_{n\text{-th order}} \frac{d^2 F_n}{d\varphi d\psi} \cdot \Delta\Omega \cdot d\left(\frac{\Delta\omega}{\omega}\right) \\ &= 174.4 NE^2 [GeV] Q[nC] \frac{f_n(K)}{n} \Delta\Omega [(\mu\text{rad})^2], (n = 1, 3, \dots). \end{aligned} \quad (4.9)$$

For x-ray alignment applications, it is sufficient to consider the undulator source spectrum as a sum of the delta function:

$$F(\omega) = 174.4 s_0 NE^2 [GeV] Q[nC] \Delta\Omega [(\mu\text{rad})^2] \cdot \sum_{m=1}^{\infty} \frac{f_{2m-1}(K)}{2m-1} \cdot \delta[\omega - (2m-1)\omega_1]. \quad (4.10)$$

When the source pinhole is inserted, only a fraction ($s_0 = 1 - e^{-a_0^2/2\sigma_0^2}$) of the photons reach the target pinhole, where σ_0 is the rms radius of the electron beam. Otherwise, we have $s_0 = 1$.

Figure 4.4 shows the function $f_n(K)/n$ for the first five odd harmonics. We note that if we choose $0.5 \leq K \leq 0.8$, the first harmonic flux is over 50% of its peak, the third harmonic is at 2 – 9% of the intensity of the first harmonic, and the fifth harmonic is at the 0.04 – 0.9% level. Furthermore, if we let the third harmonic photon energy fall above the absorption edge of the pinhole material, only the fifth and higher harmonics may penetrate the pinhole foil to produce background. Hence we will be able to use thinner foils (0.25 mm) to make pinholes. Table 4.3 summarizes our recommendation for an alignment undulator with a clean spectrum.

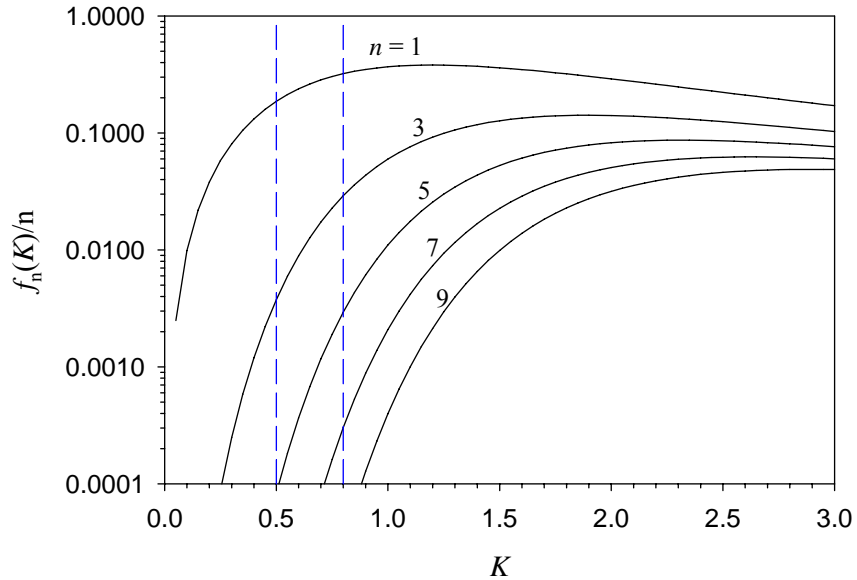


Figure 4.4: Function $f_n(K)/n$ for the first five odd harmonics.

Table 4.3: Parameters of a clean undulator for x-ray alignment

Pinhole material	Ta	W	Au
First harmonic energy $\hbar\omega_1$	≥ 22.6 keV	≥ 23.3 keV	≥ 26.6 keV
Magnetic parameter K	0.50 – 0.80	0.50 – 0.80	0.50 – 0.80

The single-electron analysis above is valid only for electron beams with very low emittance. For electron beams with large emittance, and for pinholes near the source undulator, numerical analyses to account for beam divergence and even harmonics will be needed. The program XOP [16] contains a set of useful design tools for calculating the source and optics properties.

4.4 Example: LCLS with a dedicated alignment undulator

In this example, we consider the LCLS undulator with a dedicated alignment undulator upstream of the tune-up dump, which can be removed from the beam by way of opening its gap or a roll-out mechanism. Table 4.4 shows the hardware parameters and expected performance data. Note that the electron energy and magnetic gap value are calculated to meet the requirements for K and ω_1 .

Table 4.4: Design parameters for LCLS x-ray alignment with dedicated undulator source

Electron beam	
Electron energy	9.36 GeV
Bunch charge	3.0 nC
Electron beam size	45 μm
Alignment undulator	
Period	3.0 cm
Magnetic gap	20 ~ 25 mm
Magnetic parameter K	0.6
First harmonic photon energy $\hbar\omega_1$	24.8 keV
X-ray pinholes	
Pinhole foil material	Tantalum or tungsten
Pinhole foil thickness	0.25 mm
Source pinhole diameter $2a_0$	70 μm
Target pinhole diameter $2a$	60 μm
Detector pinhole diameter	70 μm
Source pinhole transmission factor s_0	59%
Photon flux through target pinhole @ 100 m	
First harmonic flux, $F_1^{(o)}$	2.2×10^5 (ph/shot)
Third harmonic flux, $F_3^{(o)}$	8.9×10^3 (ph/shot)
Fifth harmonic flux, $F_5^{(o)}$	332 (ph/shot)
Detector	
Region of interest	8 mm \times 8 mm
Filter thickness / material	0.1 mm / Silicon

Mirror	None
Scintillator material	YAG
Scintillator thickness	1 mm
Detector efficiency at $\hbar\omega_1$	74%
Target alignment accuracy (rms)	2.5 μm or better

If we do not have a dedicated alignment undulator, the first undulator segment in the undulator assembly can be used. This approach, however, incurs many complications in x-ray optics:

- (1) The undulator used by the FEL has a high effective K value of 3.50. Hence the undulator generates rich harmonics, leading to substantial flux above 300 keV. To reduce the background, an x-ray mirror will be necessary to reduce the high-energy background, thus substantially increasing the cost and complexity of the detector system.
- (2) Since any direct hit to the thick high-Z materials in the undulator by the electron beam result in unacceptable radiation damage to the undulator magnetic structure, the electron beam will need to be steered around the pinholes and fluorescence screens. The beam offset may be ~ 1 mm and the pinhole support and fluorescence screen about 1 mm wide.
- (3) Every time a target or screen is to be inserted into the x-ray beam, the electron beam needs to be steered away from it. The complexity of this procedure increases the risk of the electron beam accidentally hitting the high-Z targets and damaging the undulator.
- (4) Finally, components in the first 20 m of the undulator assembly will not be able to take advantage of the x-ray alignment technique.

5. Fiducialization issues

So far we have established a procedure to align x-ray pinholes to a long straight line at very high accuracy. The technique would not be very useful unless we can relate the pinholes to beamline components and their functioning center point, centerline, or center plane with equal accuracy. In this section, we will discuss fiducialization techniques using conventional laboratory instruments (off-line fiducialization) and methods using the electron or x-ray beam in situ (on-line fiducialization).

5.1 Off-line fiducialization

It is common practice that prior to the installation of accelerator components the relationship between the beam axis and outside reference markers be established in a fiducialization step. During the girder assembly process these markers are then used to create the proper relative position between individual parts without having access to a representation of the beam axis. In some cases that means that reference surfaces such as the insertion device vacuum chamber outer diameter are used for assembly or the machined body of the RF BPM is used to position this device once a QC check has confirmed its accuracy. Other components such as quadrupoles and undulators require an intermediate step to establish the magnetic axes that will be used as reference for the fiducial markers. This step adds another level of uncertainty due to probe noise at low field values in determining the position accuracy of these components. For example, LCLS estimates that the quadrupole fiducials can be determined to ± 25 μm in both transverse directions while the undulator fiducials are estimated to be within ± 40 μm vertically and ± 50 μm horizontally.

Finally, all of these components are assembled on a common girder support structure utilizing a coordinate measurement machine (CMM). State-of-the-art CMMs can reach micron accuracy in a small volume of no more than several meters long. LCLS will utilize a system with a point accuracy of $\pm(2 + L[\text{m}]/350) \mu\text{m}$ in a volume of $4.5 \text{ m} \times 1.2 \text{ m} \times 1 \text{ m}$. In this case $L[\text{m}]$ represents the distance measured from the CMM coordinate origin to the measurement point in meters. Naturally that type of accuracy requires a tightly temperature-controlled measurement room.

Similarly, the pinhole assemblies can be fiducialized and integrated on the support system. Figure 5.1 shows a possible arrangement for using this new alignment concept. A number of beamline components are pre-aligned on a common girder, including two retractable pinholes, which are fiducialized in the inserted position during pre-alignment. A kinematic mount ensures micrometer reproducibility [18] of the x-ray pinhole at the inserted position. With that, it is now possible to bring the girders on the XBA one at a time.

In addition, external accessible targets have been mounted on the invar rod pinhole holder. These can be picked up with common survey instruments for local alignment or verification tasks after the XBA has been established. Having access to these references provides a perfect tie to constrain the location of the control network in the XBA system. This enhances the position accuracy for the installation of additional or replacement components once the network has been resurveyed including these external alignment targets.

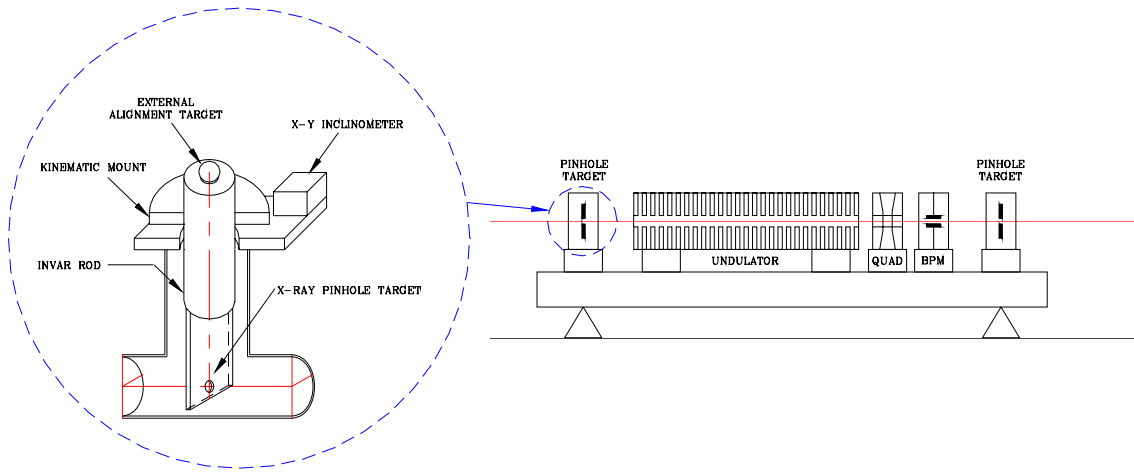


Figure 5.1: Schematic for positioning a pre-aligned girder assembly using x-ray pinhole targets. Kinematic mounted x-ray pinhole targets transfer their position information directly to an external target via an integral invar rod. An X-Y inclinometer is used to keep the invar rod axis in the coordinate plane.

5.2 Online fiducialization

As the bench fiducialization cannot provide sufficient accuracy for the most stringent applications, especially for magnetic components where the conditions on the bench (temperature, orientation, stray magnetic fields, etc.) may vary from those found on the beamline, one can think about an online fiducialization scheme that provides further improved position accuracy. Beamline components interacting with x-ray photons, such as wire scanners and

fluorescence screens, can be directly fiducialized with the alignment x-ray beam (direct fiducialization). Other components interacting with only electrons, such as beam position monitor (BPM) and optical transition radiation (OTR) screens, will have to be fiducialized with the electron beam as the transfer medium, after the position of the latter is being measured (indirect fiducialization). Since fluorescence screens interact with both electron and x-ray beams, they will be the link between the two classes of fiducialization. As a consequence, the transfer error of the screen will be inherited by all indirectly fiducialized components. Similarly, well-built, highly reproducible wire scanners can also be used to measure the electron beam position relative to the XBA.

5.2.1 Fiducialization of wire scanners in proximity of target pinholes

For wire scanners with a highly reproducible drive mechanism or a reliable encoder, it is only necessary to find the location “zero” when the wire element crosses the XBA. Figure 5.2 shows a procedure to locate this point. First find a target pinhole near the scanner and position it on the XBA using the fine alignment procedure discussed in Section 2.4. Then the wire can be scanned across the x-ray beam. The wire partially shadows the beam when passing through the small x-ray beam, producing a reduction in x-ray intensity seen by the x-ray detector at the end of the beamline. The point of maximum reduction can thus be taken as the zero position for the wire scanner. The fiducialization accuracy can be estimated to be

$$\delta_{ws} \approx \sqrt{\delta_{align}^2 + \delta_{ws,trans}^2} , \quad (5.1)$$

where δ_{align} is the alignment accuracy of the target pinhole itself, and $\delta_{ws,trans}$ is the rms transfer error for fiducializing the wire scanner and is given by

$$\delta_{ws,trans} \approx \sqrt{0.35\eta_{ws}^2 (a^2 + R^2) + \delta_{ws,rep}^2} , \quad (5.2)$$

where a and R are the radii of the target pinhole and wire, respectively, and $\delta_{ws,rep}$ is the rms error related to mechanical reproducibility of the scanning mechanism. The constant η_{ws} depends on the quality of the measurement and generally is better for high- Z wires. For wires made of low- Z material, such as carbon, the above fiducialization technique is not very effective since the wire is nearly transparent to the x-ray beam. The alternative is to attach a high- Z x-ray wire or an x-ray pinhole directly to the wire scanner as a fiducialization marker, and precisely measure the distance between the wire and marker prior to the installation of the scanner. Hence when the fiducialization marker is aligned to the XBA, the wire is at a known position.

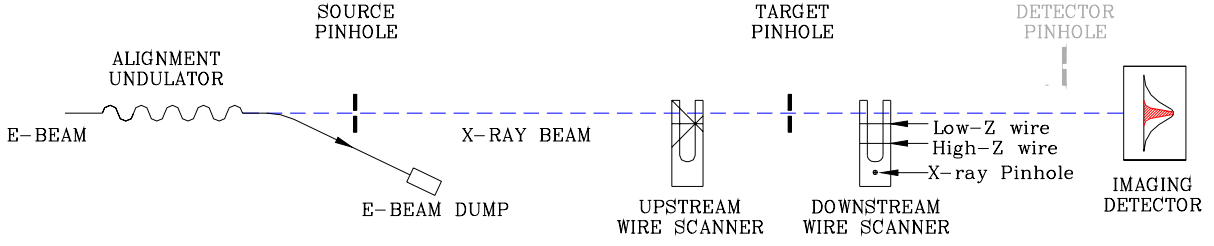


Figure 5.2: The upstream wire scanner demonstrates its fiducialization near a target pinhole using x-rays by scanning the wire across the x-ray beam after aligning the x-ray pinhole. The downstream wire scanner demonstrates that either an integral high-Z x-ray wire or an x-ray pinhole with known distances from the low-Z electron beam wire can be used as x-ray beam fiducialization markers.

5.2.2 Fiducialization of downstream fluorescence screens in proximity of target pinholes

For fluorescence screens with a highly reproducible drive mechanism or a reliable encoder, it is only necessary to find the location “zero” on the image plane where the XBA intercepts the screen. Figure 5.3 shows a procedure to locate this point: Find an upstream target pinhole near the fluorescence screen and position it on the XBA using the fine alignment procedure discussed in Section 2.4. Insert the fluorescence screen and record the image of the x-ray beam on the camera. The center of the beam spot can then be taken as the zero position for the screen. The fiducialization accuracy can be estimated to be

$$\delta_{FS} \approx \sqrt{\delta_{align}^2 + \delta_{FS,trans}^2}, \quad (5.3)$$

where $\delta_{FS,trans}$ is the rms transfer error for fiducializing the fluorescence screen and is given by

$$\delta_{FS,trans} \approx \sqrt{\eta_x^2 (0.35a^2 + \sigma_{res,x}^2) + \delta_{FS,rep}^2}, \quad (5.4)$$

where $\sigma_{res,x}$ is the resolution of the camera / optics for x-ray beam excitation, and $\delta_{FS,rep}$ is the rms error related to the mechanical reproducibility of the screen insertion mechanism. The constant η_x depends on the quality of the measurement and generally is better for higher flux. If we are using the screen immediately after fiducialization without moving the insertion mechanism, the last term in Eq. (5.4) can be omitted.

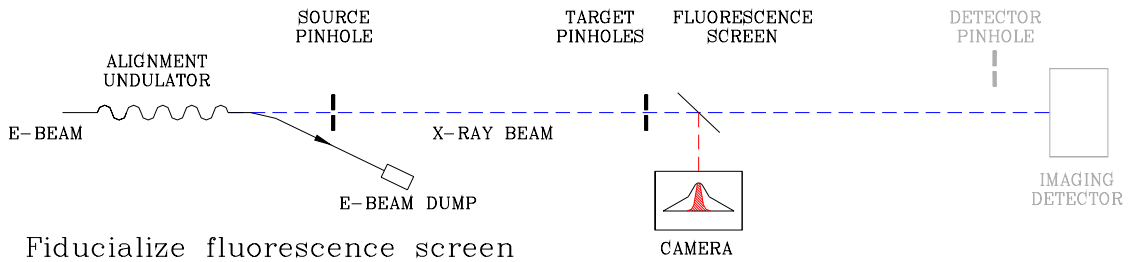


Figure 5.3: Fiducialization of a fluorescence screen near a target pinhole: Take the x-ray beam image on the fluorescence screen after aligning the x-ray pinhole.

5.2.3 Fiducialization of electron beam position monitors (BPMs, indirect)

A high-resolution electron BPM usually has good linearity within its dynamic range, but its electric center may not be on XBA. The fiducialization process determines the offset difference between the two centers. We will fiducialize the BPMs in two stages: In the first stage, we only fiducialize BPMs with a pinhole–fluorescence screen combination immediately downstream of them, using the fluorescence screen as the electron position monitor. In the second stage, we will create field-free regions between fiducialized BPMs and use them to determine the electron beam position and offsets of the BPMs in the field-free regions.

5.2.3.1 Stage 1 BPM near a fluorescence screen

We measure the offsets of BPMs located immediately upstream of a pinhole–fluorescence screen combination in three steps:

- (a) Align the x-ray pinhole (Section 2.4);
- (b) Fiducialize the fluorescence screen downstream of the BPM using the x-ray beam (Fig. 5.4A); and
- (c) Remove all pinholes, open the undulator gap, let the electron beam down the beamline, and position the electron beam's charge center on the fiducialized center of the fluorescence screen (Fig. 5.4B).

The reading on the BPM is the offset. The fiducialization accuracy can be estimated to be

$$\delta_{BPM} \approx \sqrt{\delta_{align}^2 + \delta_{BPM,trans}^2}, \quad (5.5)$$

where the rms transfer error for fiducializing the BPM $\delta_{BPM,trans}$ is given by

$$\delta_{BPM,trans} \approx \sqrt{\eta_x^2 (0.35a^2 + \sigma_{res,x}^2) + \eta_e^2 (\sigma_e^2 + \sigma_{res,e}^2) + \sigma_{BPM}^2}, \quad (5.6)$$

where σ_{BPM} is the rms resolution of the electron BPM, σ_e is the electron beam radius, $\sigma_{res,e}$ is the resolution of the camera / optics for electron beam excitation, and $\eta_e \sqrt{\sigma_e^2 + \sigma_{res,e}^2}$ is the accuracy in determining the electron beam center from the screen image. We have omitted the mechanical insertion error since we do not move the screen between x-ray fiducialization and the electron beam measurement.

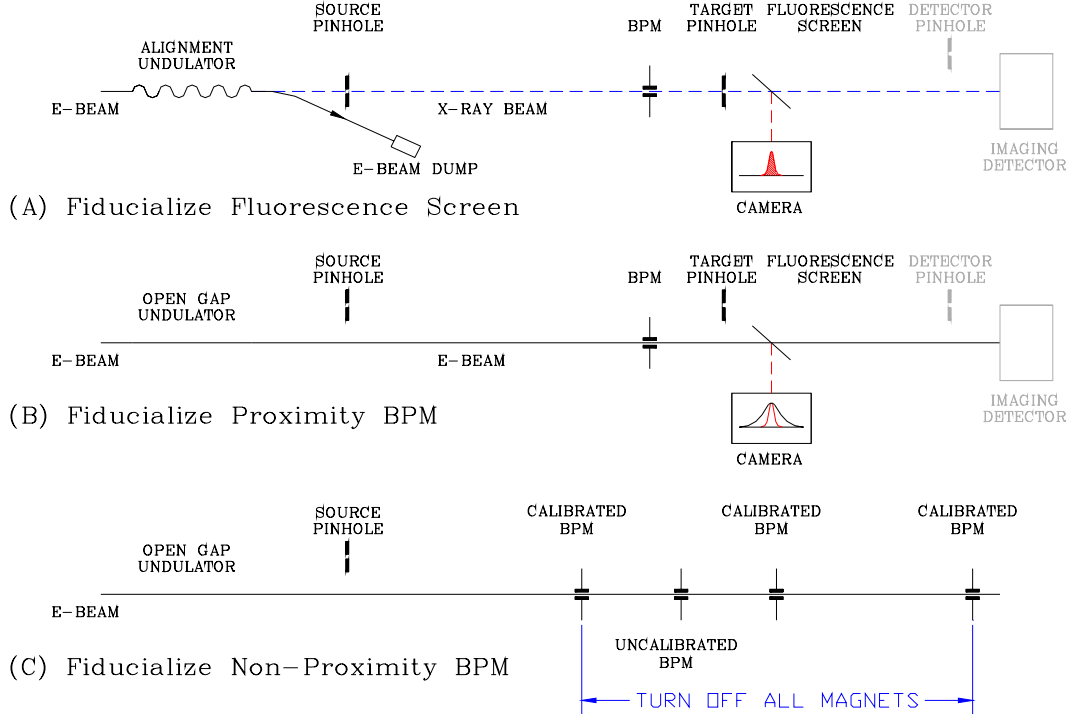


Figure 5.4: Fiducialization of electron BPMs.

5.2.3.2 Stage 2 BPM far away from fluorescence screens

In order to fiducialize BPMs at a distance from fluorescence screens, we take two already-fiducialized BPMs and turn off all magnets around them (Fig. 5.4C). If the earth's magnetic field can be neglected, the electron trajectory in the field-free region is a straight line, which can be calculated from readings of fiducialized BPMs. Hence the offset of unfiducialized BPMs in the field-free region can be determined. If the earth's field or the ambient field cannot be ignored, we will need to turn off all magnets in the region containing three or more fiducialized BPMs to calculate the curved trajectory, assuming the dipole field is uniform in the drift region. The trajectory data can then be used to determine the offsets of the BPMs in the region. The fiducialization accuracy will depend on the geometry and redundancy of the measurement.

5.2.4 Fiducialization of optical transition radiation screens (indirect)

Since OTR is only produced by charged particles, the OTR screens cannot be fiducialized directly by the x-ray beam. However, if the electron beam position is known from fluorescence screen measurements (Fig. 5.4B), we can simply substitute the fluorescence screen with an OTR screen and fiducialize the latter. A single-shot electron BPM can be used to monitor beam position jitter. The fiducialization accuracy can be estimated to be

$$\delta_{OTR} \approx \sqrt{\delta_{align}^2 + \delta_{OTR,trans}^2}, \quad (5.7)$$

where the rms transfer error for fiducializing the OTR screen $\delta_{OTR,trans}$ is given by

$$\delta_{OTR,trans} \approx \sqrt{\delta_{BPM,trans}^2 + \eta_{OTR}^2 (\sigma_e^2 + \sigma_{res,OTR}^2) + \delta_{OTR,rep}^2}, \quad (5.8)$$

where $\sigma_{res,OTR}$ is the resolution of the OTR diagnostics, $\eta_{OTR}\sqrt{\sigma_e^2 + \sigma_{res,OTR}^2}$ is the accuracy in determining the electron beam center from the OTR screen image, and $\delta_{OTR,rep}$ is the rms error related to the mechanical reproducibility of the screen insertion mechanism.

5.2.5 Alignment of quadrupole magnets

Quadrupole and sextupole magnets are used extensively as electron beam optical elements. These magnets have centerlines parallel to the electron beam axis. These magnets share two properties: (1) the magnetic field strength is zero at the magnetic center, and (2) when passing through a magnet, the deflection angle of an ultra-relativistic electron beam is inversely proportional to the momentum of the electrons, and proportional to the magnetic field strength. If the electron beam passes through the center of a magnet, the downstream electron trajectory will not change when we scan the strength of the magnetic field.

The following procedure aligns the center of a quadrupole (sextupole) magnet to XBA using field scans (Fig. 5.5):

- (a) Steer the electron beam through the fiducialized centers of the BPMs upstream and downstream of the quadrupole, or the fiducialized center of at least one BPM next to the magnet.
- (b) Vary the field strength of the quadrupole and monitor the trajectory changes downstream.
- (c) If the downstream electron trajectory changes during a field scan, move the magnet to a different point in the transverse plane and perform the field scan again, until you reach the location where the trajectory change is minimized.

The fiducialization accuracy can be estimated to be

$$\delta_{quad} \approx \sqrt{\delta_{align}^2 + \delta_{quad,trans}^2}, \quad (5.9)$$

where the rms transfer error for aligning the quadrupole $\delta_{quad,trans}$ is given by

$$\delta_{quad,trans} \approx \sqrt{\delta_{BPM,trans}^2 + \left(\frac{3.3E}{\varepsilon_Q \beta Q_0} \sigma_{BPM} \right)^2}, \quad (5.10)$$

where E is electron energy in GeV, $\beta = \sqrt{\beta_Q \beta_{BPM}}$ is the average beta function in meters, and Q_0 is the integrated quadrupole gradient in T/m. The parameter $\varepsilon_Q = (I_{max} - I_{min})/I_0$ is determined by the magnetic field scan range. The value for $\varepsilon_Q = 1$ if the quadrupole current varies from $I_{min} = 0$ to full strength $I_{max} = I_0$, while $\varepsilon_Q = 0.4$ if the current changes only $\pm 20\%$ around the operation values. We note that the additional transfer error is comparable with that of electron beam-based alignment using the field scan approach.

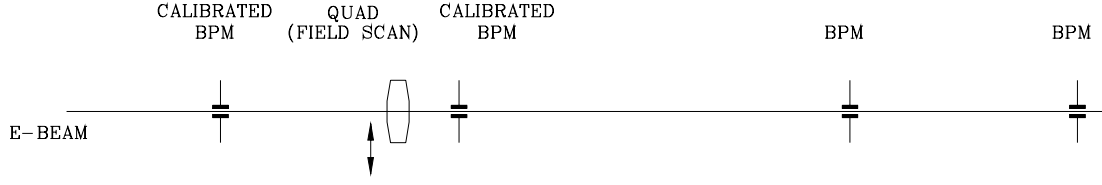


Figure 5.5: Alignment of a quadrupole magnet: search for a position where the electron trajectory is not affected by field scans.

5.2.6 Alignment of magnetic undulators (center plane)

Planar undulators are periodic magnetic dipole structures. In the plane bisecting the gap, the periodic magnetic field has a minimum amplitude. The amplitude then increases quadratically with the distance away from the center plane. This increase in magnetic field induces a spectrum shift in the spontaneous radiation. By moving the electron trajectory relative to the undulator, a spatial resolution of $\sim 10 \mu\text{m}$ can be obtained using appropriate x-ray optics, especially when differential measurements are performed against a standard undulator [19].

5.2.7 An example: LCLS undulator

Table 5.1 summarizes the estimated alignment errors for the LCLS undulator components.

Table 5.1: RMS XBBA accuracy for LCLS undulator components

Component	Transfer error	Alignment accuracy	Notes
Target pinhole	N/A	$2.5 \mu\text{m}$	$\eta_x = 0.1$, $a = 30 \mu\text{m}$, $a_0 = 30 \mu\text{m}$, and $a_D = 30 \mu\text{m}$
Wire scanner	$2.0 \mu\text{m}$	$3.2 \mu\text{m} + \text{mech.}^*$	$R = 15 \mu\text{m}$, $\eta = 0.1$
Fluorescence screen	$2.0 \mu\text{m}$	$3.2 \mu\text{m} + \text{mech.}^*$	$\sigma_{res,x} = 10 \mu\text{m}$, $\eta = 0.1$
BPM	$3.8 \mu\text{m}$	$4.5 \mu\text{m}$	$\sigma_{res,e} = 40 \mu\text{m}$, $\sigma_e = 45 \mu\text{m}$, $\sigma_{BPM} = 1 \mu\text{m}$, $\eta_e = 0.05$
OTR screen	$6.0 \mu\text{m}$	$6.5 \mu\text{m} + \text{mech.}^*$	$\sigma_{res,OTR} = 10 \mu\text{m}$, $\sigma_e = 45 \mu\text{m}$, $\eta = 0.1$
Quadrupole magnet	$< 5 \mu\text{m}$	$< 7 \mu\text{m}$	$E = 13.6 \text{ GeV}$, $Q_0 = 3 \text{ T}$, $\beta = 10 \text{ m}$, $\varepsilon_Q = 0.35$
Undulator	$\sim 10 \mu\text{m}$	$\sim 10 \mu\text{m}$	Field error dependent, vertical only

* mech. = Errors associated with mechanical reproducibility

6. Further discussions

In this section, we will discuss several practical issues related to the application of x-ray beam alignment and further enhancement of the technique.

6.1 Relation with electron beam-based alignment

Let us consider a magnetic lattice consisting of only quadrupole magnets. When all centers of the magnets are aligned on a straight line and the electron beam travels along the line, the electron trajectory is independent of beam momentum or magnetic field strength. Otherwise, when scanning the electron energy or the strengths of the magnet fields, the trajectory will change, giving telltale signs of the misalignment and clues for correction. By correctly interpreting the trajectory changes during energy scans or field scans, the electron beam-based alignment (EBBA) technique has matured in the past decade, and can attain micron accuracy under ideal conditions [20, 21]. However, the EBBA technique is sensitive to the presence of a dipole field that cannot be turned off during the alignment process. Even the earth's field can adversely affect the outcome. Other engineering limitations may also come into play. For example, a slight asymmetry of a magnet's core may generate an unintentional dipole magnet within and move the magnetic center during magnet field scans. Finally, since no fixed monument is used to define the EBA, it is not predetermined to what line the final convergence will lead. Hence the EBA cannot be accurately reproduced after magnets are moved.

The x-ray beam-based alignment (XBBA) can enhance the EBBA in two aspects:

- (A) Using the fiducialization / alignment technique described in the previous section, all magnetic quadrupoles and undulators can be positioned within several micrometers from the XBA, providing the EBBA with an excellent starting configuration.
- (B) By forcing the EBA to coincide with the XBA, we obtain a high reproducibility inherently lacking in the EBBA. This can be achieved in several ways: (1) Start from a configuration near the XBA that imposes appropriate constraints during the entire EBBA process (such as a range of allowable small changes in BPM offsets) to prevent the EBA from wandering too far from the XBA. (2) Multiple fluorescence screen measurements (Fig. 5.3) along the accelerator can be used to show differences between the two axes after EBBA convergence. If a systematic deviation is found, the entire beamline can be rotated to force the EBA to coincide with the XBA. When this is accomplished, the user experiments can enjoy reproducible beam position and direction from one run to the next.

When the undulators' first field integrals exceed the threshold values, the EBBA in the undulator hall will not be able to converge to a straight line. Hence the XBA may be used as a quality control tool to monitor the final EBA to prevent this from happening. In the rare case when the EBBA does not converge, the XBA provides a fall-back position.

6.2 Extension of XBA to user area

From Section 3, we can see that the RMS alignment error increases as the square root of the distance between the source and detector pinholes. Hence the main beamline should be kept as short as possible, containing only those components requiring critical alignment plus an adequate working distance up- and downstream of the main undulator section. In order to align the x-ray

transport line and the user beamline components, we need to extend the alignment monuments for XBA beyond the detector pinhole. The following procedure may be used for this purpose (Fig. 6.1):

- (A) Install two or more alignment monument / pinhole assemblies in the transport line and user experiment area.
- (B) Set up the alignment undulator (Section 2), and insert the source and detector pinholes.
- (C) Remove the imaging detector behind the detector pinhole, and set up another imaging detector / PSD at the end of the experiment area. Fiducialize the new detector using the x-ray beam spot there.
- (D) Insert the last alignment monument and move it to center the beam spot on the detector plane.
- (E) Retract the old detector pinhole.

The XBA is now extended up to the last monument pinhole. Other pinholes and monuments can be aligned using the procedure described in Section 2, with the last monument pinhole serving as the new detector pinhole. Note that the monuments established with this procedure have slightly poorer accuracy than the pinholes inside the accelerator. In most cases however, it is not a major problem since the transport line and user beamline usually require less stringent alignment in the machine coordinates.

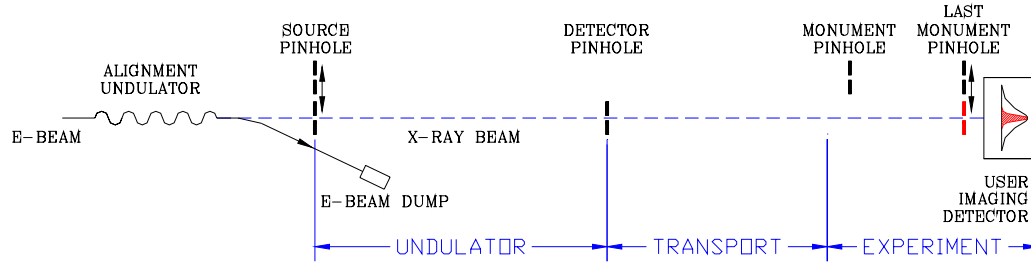


Figure 6.1: Extension of XBA into transport and user experimental area.

We note that the extension of the XBA into the x-ray beamline is especially important for x-ray diagnostics of the undulator and the FEL, since the x-ray alignment sets up an absolute angle reference for the undulator radiation pattern, enabling diagnostics of the electron trajectory within the magnetic structure of the undulator.

6.3 Enhancement of positioning accuracy with zone plate targets

From Section 3, we note that the optimum target pinhole size increases as the square root of the beamline length S and x-ray wavelength λ . It follows that the area of the pinhole increases linearly with the beamline length, and its acceptance solid angle for x-ray photons remains unchanged. Hence the photon statistic is independent of the beamline length. However, the enlargement of the target pinhole in longer accelerators or lower energy machines (longer x-ray wavelength) does increase the alignment error.

In these cases, one may consider using Fresnel zone plates to improve the positioning accuracy. Figure 6.2 shows the calculated x-ray beam spot size at the detector plane. See Appendix B for details. A phase zone plate with even a handful of zones (≥ 4) can improve the resolution over the optimal pinhole by a factor of three or more. If zone plates are used as alignment targets, the practical considerations of zone plate fabrication will likely drive other design issues of the entire x-ray optics system. We will discuss this in a separate paper.

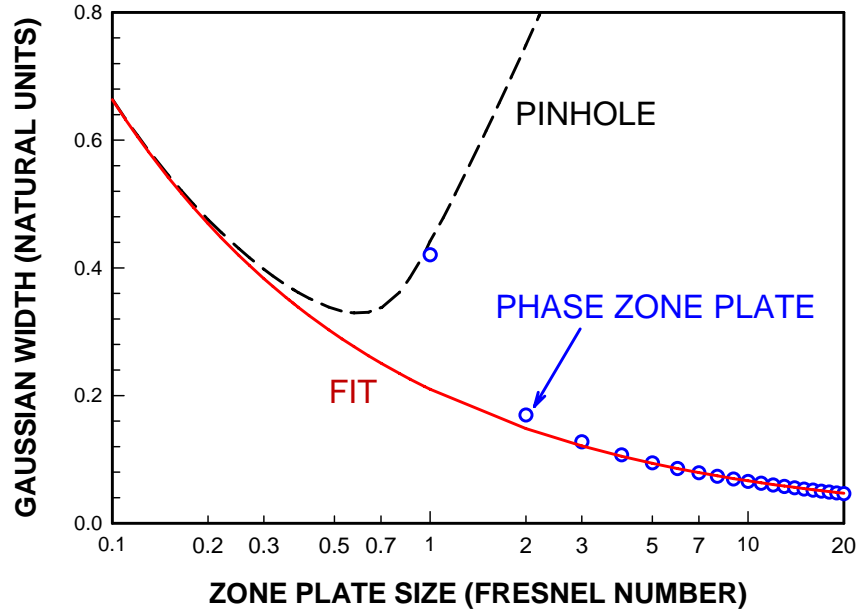


Figure 6.2: X-ray PSF profile width at the detector plane: (Circle) phase zone plates, (dashed line) pinhole, and (solid line) fit for high Fresnel number cameras.

6.4 Mechanical engineering issues and real-time position feedback

To implement the technique proposed in this work and to obtain micron accuracy, we are facing significant challenges in mechanical engineering:

- (A) The source and detector pinholes are the master alignment monuments when inserted in the x-ray beamline. They are the two most important components for x-ray alignment. The positions of the entire XBA, EBA, and hence all accelerator components between the two monuments are defined by them. Their positions need to be carefully chosen, their supports need to be carefully designed, and their insertion mechanisms need to be accurately engineered to allow greatest reproducibility and longest non interrupted service.
- (B) In order to transfer the accurate position information from the pinholes to the attached component(s), the target insertion mechanism needs to have comparably high reproducibility. State-of-the-art kinematic mounts with submicron accuracy at high load (> 100 N) need to be employed. In addition, the repeatability of the retractable pinholes is a major source of error for transferring the position information to an outside fiducial as

shown in Figure 5.1. Hence ultrahigh-precision machining and motion systems are required.

- (C) For fiducialized screens and wire scanners to be useful as beam position monitors, not only should their motion resolution be finer than the required accuracy, but their motion reproducibility should also be adequate. Currently available nano-positioning systems may have to be utilized.
- (D) To realize micrometer positioning accuracy for accelerator components, the support and mover system of the component(s) attached to the pinhole target need to provide a smooth motion and have a resolution finer than the required accuracy. In particular, the pinhole location should closely match the location of the actuation system in order to obtain a one-to-one motion ratio with respect to the pinhole. This will minimize the number of iterations necessary to bring both ends of the component onto the XBA.
- (E) To maintain micrometer positioning accuracy for accelerator components, the support and mover system of the component(s) needs to be stable, and loads need to be carefully distributed. For example, it is highly desirable to separate supports of quadrupole magnets and BPMs, which have very high stability requirements but no moving parts, from those of heavy undulators, which have less stringent stability requirements but need to be rolled in and out at the LCLS or opened and closed in other facilities.

Even when the mechanical design meets all these challenges, environmental changes may still be beyond human control. A temperature change of 1°C can easily move the target on a 1-m support by $10\text{ }\mu\text{m}$ or more. The temperature variation of the floor, the wall, and the support stand will easily move parts over a micrometer scale. Even if we have the enclosure temperature under rigorous control, the daily tidal motion of the crust will move the ground up and down by up to $\pm 30\text{ cm}$ in a 12-hour period, resulting in some twisting and bending of the floor. While the magnitude of the twisting and bending depends on local geological conditions, a reproducible alignment literally depends on the phase of the moon.

If the ground motion is not acceptable after applying passive mitigation approaches, a real-time position feedback system needs to be considered. Figure 6.3 shows a possible implementation using an off-axis x-ray alignment beamline. The electron beam is steered through a chicane or a two-stage trajectory offset before entering the main undulator hall. The offset of the two beams are adjustable from zero to a maximum of several millimeters. Each critical component will have two independently retractable pinhole targets, one on-axis and the other off-axis, in the monitor beamline. The monitor beamline is parallel to the EBA and has its own independently operated source and detector pinholes, as well as its own detector system.

During the on-axis alignment procedure (Fig. 6.3A), the trajectory offset is set to zero and the on-axis target is used to position the critical component (Section 2). After the alignment is completed, we set the offset electron trajectory to be collinear with the monitor beamline (Fig. 6.3B). The same undulator now produces x-ray beam along the parallel monitor beam axis, which can be used to fiducialize the off-axis monitor pinhole target without moving the component. From now on, any change in the position of the off-axis target pinhole will shift the pinhole camera image on the detector, providing real-time information on the component motion at a resolution of micrometers. The information will allow position adjustments to be made while

the accelerator is running. Since only one target is inserted at any one time, the wakefield effect of the target may be neglected. However, to use such a feedback system for position control of an x-ray FEL, a larger separation of the two beamlines, even separate beam pipes, may be required to avoid contamination of the position monitor signal by the FEL beam.

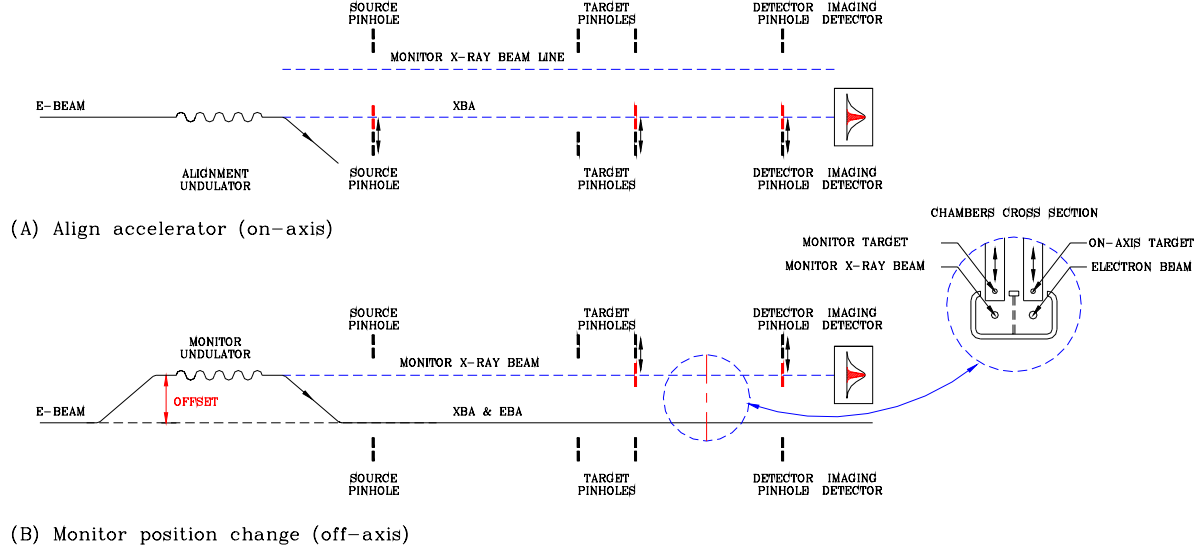


Figure 6.3: Real-time position monitoring system: (A) Alignment with on-axis trajectory and targets. (B) Observe position change with off-axis monitoring x-ray beamline. The inset shows two independently retractable pinhole targets, one used for XBA and the other for monitoring position changes. In x-ray FEL, the monitoring beamline has its own vacuum chamber to reduce the radiation background.

7. Summary and conclusion

We proposed a new alignment technique using an undulator x-ray beam produced by high-energy electrons. The proposal contains two major technical components: First, two solidly built x-ray pinholes (source and detector) are used to define a highly stable and reproducible x-ray beam axis (XBA). Second, the XBA is chosen to be collinear with the electron beam axis in order to minimize the transfer errors to accelerator components and maximize the coincidence between x-ray beam and e-beam.

We showed that a measurement accuracy of $1 - 3 \mu\text{m}$ can be achieved for target pinholes in the 200-m-long LCLS undulator hall. The accuracy can be further enhanced with x-ray zone plate targets if necessary. We described procedures to transfer this position information in situ to quadrupoles, diagnostic components, undulators, and user beamlines, at an accuracy of better than $10 \mu\text{m}$ in the case of the LCLS undulator.

This x-ray alignment technique also enhances the electron-beam based alignment (EBBA) process in three aspects: First, it provides a good starting configuration for the EBBA. Second, it provides fixed anchors for the electron beam axis (EBA) for reproducible trajectories from run to run. Last but not least, it facilitates the extension of the coordinate axes into the user area at high

accuracy, enabling far-field x-ray diagnostics to perform angular distribution measurements with absolute angle reference.

Although we used the LCLS parameters for this paper, other FELs currently in the design stage could benefit by integrating such a system from the beginning. The proposed alignment system promises superior alignment accuracy over long distances and may therefore be a viable approach for aligning the International Linear Collider (ILC) currently under consideration.

8. Acknowledgement

We would like to thank Steve Milton for his encouragement for this work. This work is supported by the U.S. Dept. of Energy Office of Basic Energy Sciences, Office of Science, under contract numbers W-31-109-ENG-38 and DE-AC03-76SF00515.

9. References

- [1] J. Arthur et al., “LCLS Conceptual Design Report,” SLAC-R-593, <http://www.ssl.slac.stanford.edu>.
- [2] J. Pflüger, “Undulator systems for the X-FEL,” DESY-HASYLAB. Workshop on Undulator Systems for X-FELs, WUS2005 at DESY Hamburg, Germany, June 6-8, 2005.
- [3] T. Shintake, “Soft-X-Ray SASE-FEL Project at Spring-8,” Proceedings of the Second Asian Particle Accelerator Conference, Beijing, China, September 17-21, 2001, p. 248, <http://www.jacow.org>.
- [4] Yujong Kim et al., “Start-To-End Simulations for the PAL XFEL Project,” Proceedings of the Third Asia Particle Accelerator Conference, Gyeongju, Korea, March 22-26, 2004, to be published at <http://www.jacow.org>.
- [5] W. B. Herrmannsfeldt, M. J. Lee, J. J. Spranza, K. R. Trigger, “Precision Alignment Using a System of Large Rectangular Fresnel Lenses,” *Applied Optics* **6** (7), (1968).
- [6] L. V. Griffith, R. F. Schenz, G. E. Sommergren, “Magnetic alignment and the Poisson alignment reference system,” *Rev. Sci. Instrum.* **61** (8) (1990).
- [7] Ioan Feier, Horst Friedrichs, Merrick Penicka, “The Poisson Alignment Reference System Implementation at the Advanced Photon Source,” Proceedings of the International Workshop on Accelerator Alignment, Argonne National Laboratory, 1997.
- [8] A. E. Siegman, *Lasers*, (University Science Books, Mill Valley, CA, 1986).
- [9] M. Borland, “A Method for Calculating Emittance from Undulator Images,” SSRL ACD-NOTES 60, 1989.
- [10] B.X. Yang and A. Lumpkin, “Simultaneous Measurements of Electron Beam Size and

- Divergence with an Undulator,” Proceedings of the 1999 Particle Accelerator Conference, New York, NY, p. 2161, <http://www.jacow.org>.
- [11] B.X. Yang, “Optical System Design for High-Energy Particle Beam Diagnostics,” BIW’02, Uptown, New York, May 6-9, 2002, AIP Conf. Proc. **648**, p. 59 (2002).
 - [12] P. Elleaume, C. Fortgang, C. Penel, E. Tarazona, “Measuring Beam Sizes and Ultra-Small Electron Emittances Using an X-Ray Pinhole Camera,” J. Synch. Rad. **2**, 209 (1995).
 - [13] C. Zai et al., “Beam Size Measurement of the Stored Electron Beam at the APS Storage Ring Using Pinhole Optics,” Rev. Sci. Instrum. **67**, 3368 (1996).
 - [14] H. Nuhn, “LCLS Undulator Requirements,” LCLS Specification 1.4-001.
 - [15] J. Kirz et al., X-ray Data Booklet, and references cited therein, Lawrence Berkeley Lab, Berkeley, CA, 1986.
 - [16] M. Sanchez del Rio and R. J. Dejus, “XOP: Recent Developments,” SPIE Proceedings **3448**, pp. 340-345 (1998).
 - [17] K. J. Kim, “Characteristics of Synchrotron Radiation,” AIP Conf. Proc. **184**, New York, NY, 1989.
 - [18] A. Slocum, “Design of Three-Groove Kinematic Couplings,” Precision Engineering **14**, pp. 67-73 (1992).
 - [19] B. X. Yang, “High-Resolution Undulator Measurements Using Angle-Integrated Spontaneous Radiation,” Proceedings of the 2005 Particle Accelerator Conference, Knoxville, TN, p. 2342, <http://www.jacow.org>.
 - [20] Chris Adolphsen et al., “Beam Based Alignment Technique for the SLC Linac,” Proceedings of the 1989 Particle Accelerator Conference, Chicago, IL, Mar 20-23, 1989, p. 977, <http://www.jacow.org>.
 - [21] P. Tenenbaum and T. O. Raubenheimer, “Resolution and Systematic Limitations in Beam Based Alignment,” Phys. Rev. ST Accel. Beams **3**, 052801 (2000).

Appendix A: Fresnel Diffraction of a Circular Aperture

Let us consider the diffraction geometry shown in Figure 3.1. A circular aperture is placed at a distance S_1 from the source, and a camera at a distance S_2 from the pinhole. According to Huygens Principle, the light amplitude distribution at the camera is given by

$$E(x_2, y_2) = \frac{C}{S_1 S_2} e^{ik(S_1+S_2)} \int \exp \left\{ ik \left[\frac{x_1^2 + y_1^2}{2S_1} + \frac{(x_1 - x_2)^2 + (y_1 - y_2)^2}{2S_2} \right] \right\} dx_1 dy_1, \quad (\text{A.1})$$

where $k = \frac{1}{\lambda}$ is the wave number of the x-ray photons. Letting $\frac{1}{f} = \frac{1}{S_1} + \frac{1}{S_2}$ and $M = \frac{S_2}{S_1}$, we have $S_1 = \frac{M+1}{M} f$ and $S_2 = (M+1)f$. After making substitutions $x_i = r_i \cos \theta_i$ and $y_i = r_i \sin \theta_i$, ($i = 1, 2$), the above expression can be rewritten as

$$E(x_2, y_2) = \frac{C e^{ik(S_1+S_2)}}{S_1 S_2} \int \exp \left\{ ik \left[\frac{r_1^2}{2f} + \frac{r_2^2}{2f(M+1)} - \frac{r_1 r_2 \cos(\theta_1 - \theta_2)}{f(M+1)} \right] \right\} r_1 dr_1 d\theta_1. \quad (\text{A.2})$$

Integrating over θ_1 , we have

$$E(x_2, y_2) = \frac{2\pi C}{S_1 S_2} e^{i \left(\frac{S_1+S_2}{\lambda} + \frac{r_2^2}{2\lambda f(M+1)} \right)} \int_0^a J_0 \left(\frac{2\pi r_1 r_2}{\lambda f(M+1)} \right) e^{i \frac{r_1^2}{2\lambda f}} r_1 dr_1. \quad (\text{A.3})$$

Now we define natural units at the pinhole and image plane,

$$u_1 = \frac{x_1}{\sqrt{\lambda f}}, \quad v_1 = \frac{y_1}{\sqrt{\lambda f}}, \quad \rho_1 = \frac{r_1}{\sqrt{\lambda f}}, \quad (\text{A.4})$$

$$u_2 = \frac{x_2}{(M+1)\sqrt{\lambda f}}, \quad v_2 = \frac{y_2}{(M+1)\sqrt{\lambda f}}, \quad \text{and} \quad \rho_2 = \frac{r_2}{(M+1)\sqrt{\lambda f}}, \quad (\text{A.5})$$

and have

$$E(\rho_2) = \frac{2\pi \lambda f C}{S_1 S_2} e^{i \left(\frac{S_1+S_2}{\lambda} + \pi \rho_2^2 (M+1) \right)} \int_0^{\sqrt{F}} J_0(2\pi \rho_1 \rho_2) e^{i\pi \rho_1^2} \rho_1 d\rho_1 = E_0 \int_0^{\pi F} J_0(\rho_2 \sqrt{4\pi t}) e^{it} dt, \quad (\text{A.6})$$

where $F = a^2 / \lambda f$ is the Fresnel number of the aperture. The radial intensity distribution or point spread function (PSF) is given by the following equation.

$$I(\rho_2) = |E(\rho_2)|^2 = I_0 \left[\int_0^{\pi F} J_0(\rho_2 \sqrt{4\pi t}) e^{it} dt \right]^2. \quad (\text{A.7})$$

Figure A-1 shows the PSF graphs for different Fresnel numbers F .

The annular diffraction pattern $I(\rho_2)$ can be used to derive the integrated x -profile

$$P(u_2) = 2 \int_{|u_2|}^{\infty} \frac{I(\rho_2) \rho_2}{\sqrt{\rho_2^2 - u_2^2}} d\rho_2. \quad (\text{A.8})$$

The profile features a central peak with several side peaks and can be fitted to a Gaussian function (Fig. A-2),

$$P_{fit}(x_2) = P_0 e^{-\frac{x_2^2}{2\sigma_{2,Fresnel}^2}}. \quad (\text{A.9})$$

Figure A-3 shows the fitted (Gaussian) profile width as a function of aperture size (Fresnel number), which can be fitted to an expression similar in form to the hybrid model,

$$\frac{\sigma_{2,reso}^2}{(M+1)^2 \lambda f} = \frac{F}{3} \left(1 + \frac{1.5}{F} \right)^{-1} + 0.044 \left(0.3 + \frac{1}{F} \right). \quad (\text{A.10})$$

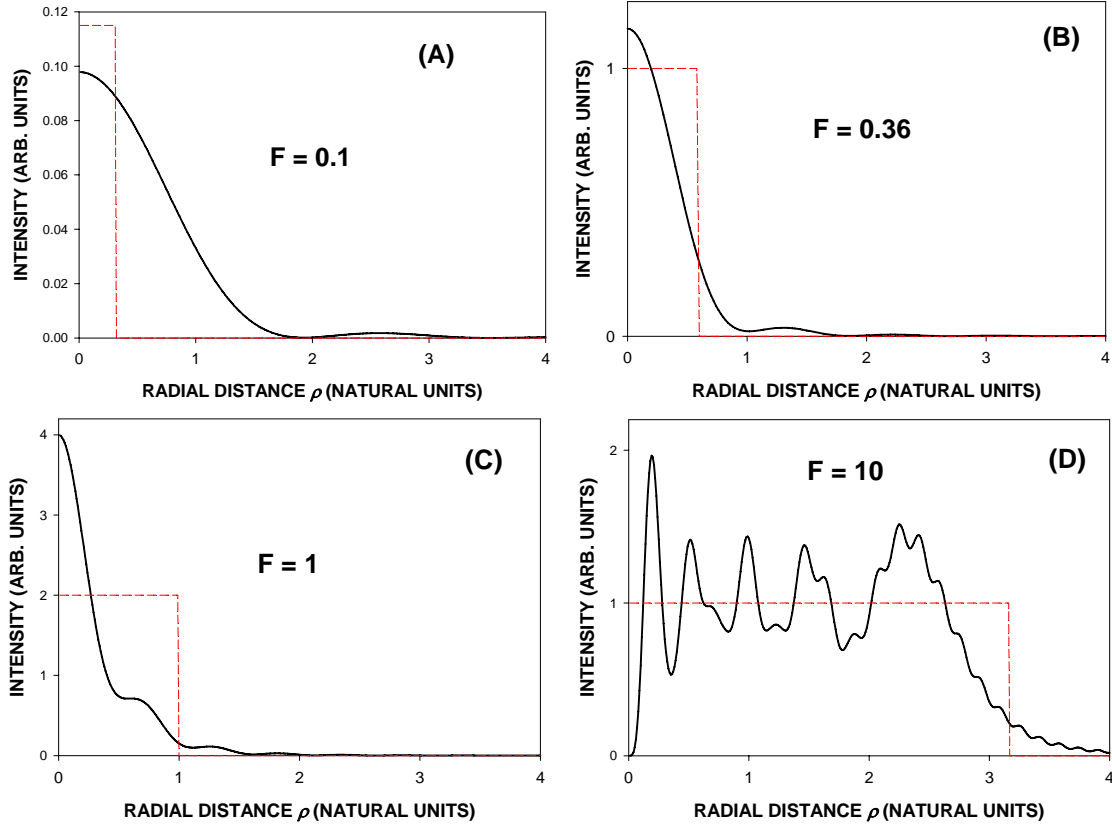


Figure A-1: Solid curves show the radial intensity distribution of the Fresnel diffraction pattern from circular apertures. Dashed lines show the geometric projection of the same aperture. The sizes of the aperture are given by their Fresnel numbers as labeled.

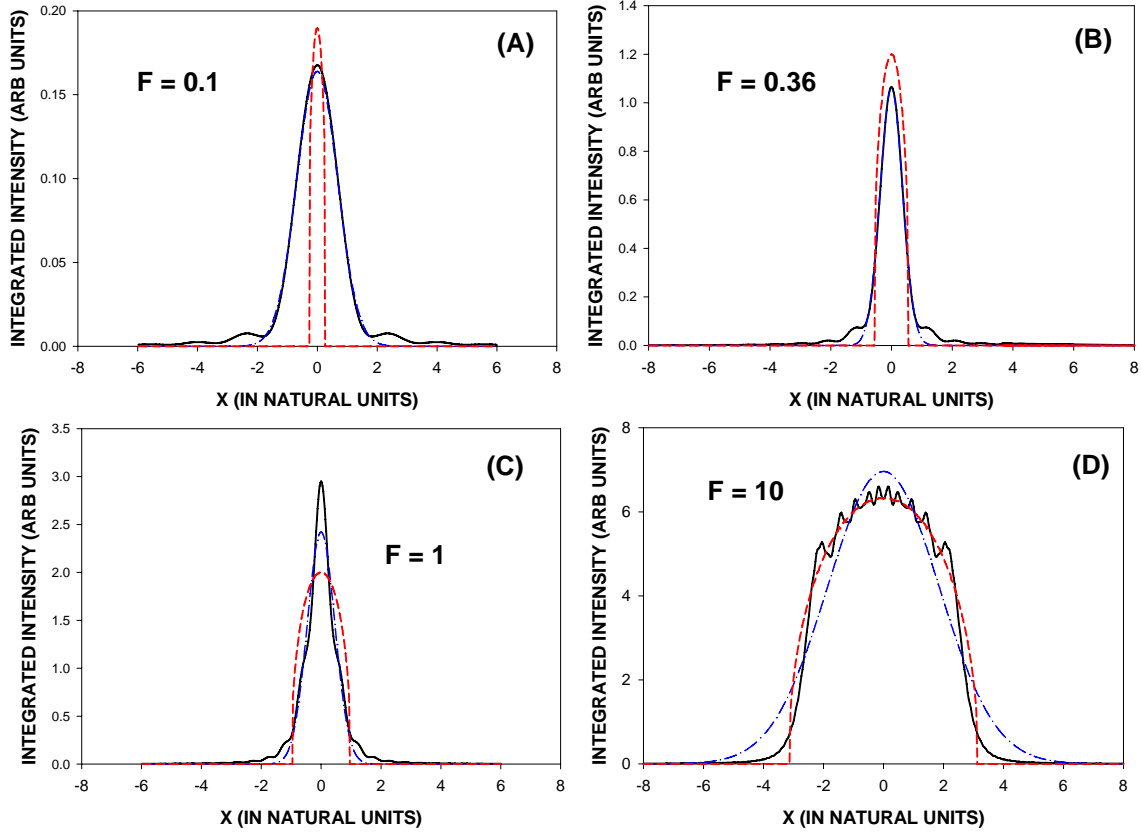


Figure A-2: The solid curves show the vertically integrated intensity profiles (PSF) of Fresnel diffraction. The dashed lines show the profiles for geometric projection of the same aperture. The dash-dot curves show the Gaussian fit to the diffraction profiles. The sizes of the aperture are given by their Fresnel numbers as labeled.

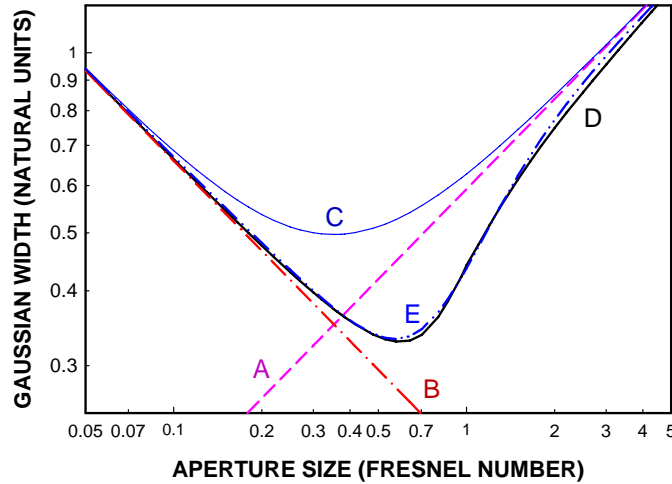


Figure A-3: Calculated Gaussian width of image profiles of a pinhole camera with different models: (A) geometric projection, (B) Fraunhofer diffraction, (C) hybrid model: quadrature sum of the previous two, (D) monochromatic Fresnel diffraction, and (E) fit to D, given by Eq. (A.6).

Appendix B: Diffraction Profile of a Fresnel Zone Plate

In this note we replace the aperture in Appendix A with a zone plate. The zone plate has F zones. Following the derivations in Appendix A, we have

$$E(\rho_2) = E_0 \int_0^{\pi N} J_0(\rho_2 \sqrt{4\pi t}) T(t) e^{it} dt, \quad (\text{B.1})$$

where the transmission function of the zone plate $T(t)$ is given by

$$T(t) = \begin{cases} 1, & 2k \leq t < 2k+1 \\ \tau, & 2k+1 \leq t < 2k+2 \end{cases} \quad (k = 0, 1, 2, \dots). \quad (\text{B.2})$$

For $\tau = 0$, the zone plate is called an amplitude zone plate (AZP). For $\tau = -1$, it is called a phase zone plate (PZP). Equation (B.1) can be rewritten for an amplitude zone plate as

$$E(\rho_2) = E_0 \sum_{k=0}^{\frac{F-1}{2}} \int_{2k\pi}^{\frac{F-1}{2}(2k+1)\pi} J_0(\rho_2 \sqrt{4\pi t}) e^{it} dt, \quad (\text{AZP}). \quad (\text{B.3})$$

The radial intensity distribution, or point spread function (PSF) for an AZP is thus given by

$$I(\rho_2) = |E(\rho_2)|^2 = I_0 \left[\sum_{k=0}^{\frac{F-1}{2}} \int_{2k\pi}^{\frac{F-1}{2}(2k+1)\pi} J_0(\rho_2 \sqrt{4\pi t}) e^{it} dt \right]^2, \quad (\text{AZP}). \quad (\text{B.4})$$

Similarly, we have the radial intensity distribution or PSF for a phase zone plate

$$I(\rho_2) = |E(\rho_2)|^2 = I_0 \left[\sum_{k=0}^{\frac{F-1}{2}} (-1)^k \int_{k\pi}^{(k+1)\pi} J_0(\rho_2 \sqrt{4\pi t}) e^{it} dt \right]^2, \quad (\text{PZP}). \quad (\text{B.5})$$

Figure B-1 shows the PSF for several zone plates with Fresnel numbers up to 40. Similarly, we can use Eq. (A.7) to derive the integrated x -profile. The profile features a central peak with diffuse background (Fig. B-2). The background from an amplitude zone plate is about twice that of a phase zone plate. In deriving the Gaussian width from the profiles, we added a background term in the Gaussian expression:

$$P_{fit}(x_2) = P_0 e^{-\frac{x_2^2}{2\sigma_{2,Fresnel}^2}} + P_B. \quad (\text{B.6})$$

Depending on the width of the calculated data region, the background term reduces the fitted Gaussian width slightly. Figure B-3 shows the Gaussian width as a function of the zone plate's Fresnel number. A simple expression can be used to approximate the resolution of a high Fresnel number zone plate camera:

$$\frac{\sigma_{2,reso}^2}{(M+1)^2 \lambda f} = \frac{0.044}{F}. \quad (\text{B.7})$$

The same expression is a good approximation for a small pinhole in the Fraunhofer regime.

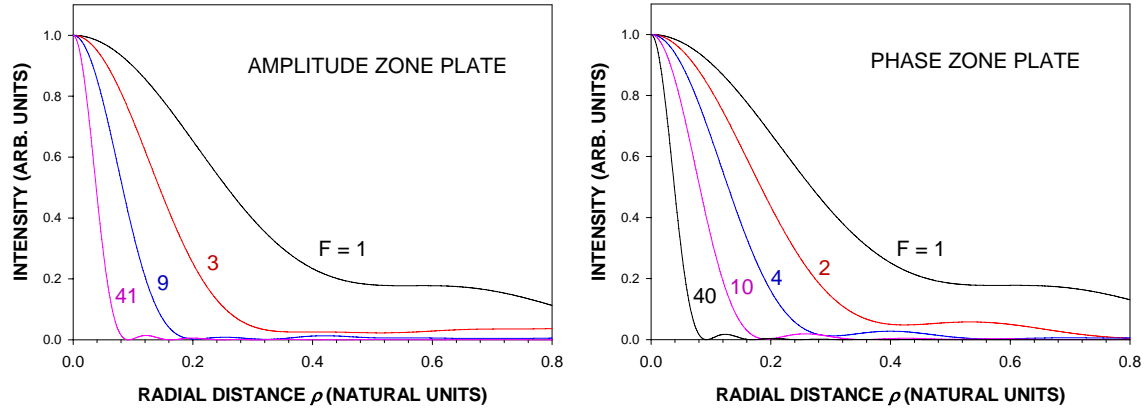


Figure B-1: Radial intensity distributions of Fresnel diffraction from circular zone plates.

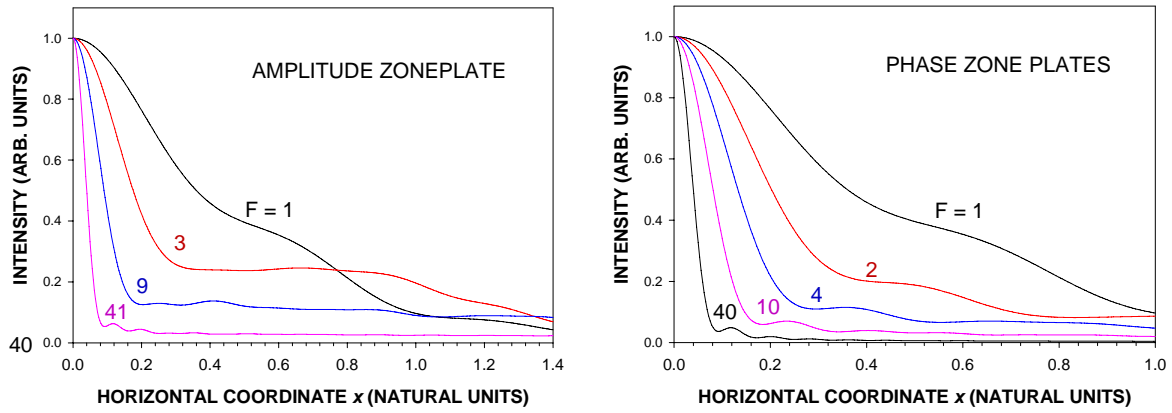


Figure B-2: Vertically integrated intensity profiles of Fresnel diffraction from circular zone plates.

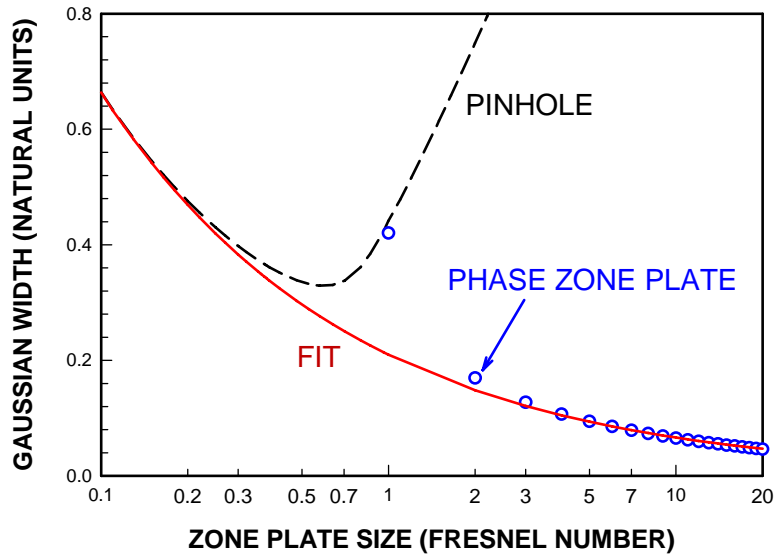


Figure B-3: Calculated Gaussian width of image profiles of a zone plate camera: (Circle) phase zone plates, (dashed line) pinhole, and (solid line) fit for high Fresnel number cameras.